Gondwana Research 70 (2019) 1–24

Contents lists available at ScienceDirect

Gondwana Research

journal homepage: www.elsevier.com/locate/gr

The 2.0–1.88 Ga Paleoproterozoic evolution of the southern Amazonian Craton (Brazil): An interpretation inferred by lithofaciological, geochemical and geochronological data

M. Roverato [a,b,*], D. Giordano [c,d], T. Giovanardi [e], C. Juliani [b], L. Polo [b]

[a] YachayTech University, School of Geological Sciences and Engineering, Hacienda San José, Urcuquí, Ecuador
[b] Instituto de Geociências (IGC), Universidade de São Paulo, INCT – Geociam, SP 05508080, Brazil
[c] Universitá degli studi di Torino, Dipartimento di Scienze della Terra, via Valperga Caluso 35, 10125 Torino, Italy
[d] Centro Nazionale delle Ricerche (CNR), Istituto di Geoscienze e Georisorse (IGG), via G. Moruzzi 1, 56124 Pisa, Italy
[e] Universitá di Modena e Reggio Emilia, Dipartimento di Scienze Chimiche e Geologiche, 41125 Modena, via Campi 103, Italy

ARTICLE INFO

Article history:
Received 20 June 2018
Received in revised form 10 December 2018
Accepted 21 December 2018
Available online 31 January 2019

Handling Editor: A.S. Collins

Keywords:
Paleoproterozoic volcanism
Amazonian craton
Fissure eruption
Felsic volcanism
Lithofacies analyses

ABSTRACT

The study of Paleoproterozoic rocks is crucial for understanding Earth's tectonic evolution during the time when most of the modern crust and ore deposits were formed. The rocks of the Brazilian Amazonian Craton record some of the most-complete and best-preserved Paleoproterozoic magmatic and volcanic episodes on Earth. Following previous investigations, we present new lithofaciological and stratigraphic records of the felsic rocks of the Tapajós Mineral Province (TMP) (~2–1.88 Ga) and the São Felix do Xingú region (SFX) (~1.88 Ga) which, combined with new petrological and geochronological data, help providing a more complete understanding of the tectonic, magmatic and volcanological evolution of the Amazonian Craton. This magmatism/volcanism is thought to be formed in a late-/post-orogenic to extentional regime confirmed by the new geochemical data presented here. The transition from late-convergent to extensional tectonic setting could register the beginning of the taphrogenesis that marked the Amazonian Craton throughout the Mesoproterozoic. The volcanological approach of this contribution can serve as a strategy for the modelling of the evolution of Precambrian volcano-sedimentary basins around the world. The large amount of rocks analyzed are divided into primary and secondary volcaniclastic products depending on if they resulted from a direct volcanic activity (pyroclastic) or processes that reworked pyroclastic fragments. Furthermore, the deposits are subdivided into massive and stratified, depending on their primary mechanisms of transport and emplacement. By confirming the results from previous studies, our study permits to depict a more precise paleo-environmental picture of the processes that occurred in the Amazonian Craton during the Late-Paleoproterozoic. In particular, the presence of large regional-scale fissural systems and caldera collapses produced large silicic explosive volcanic eruptions, also accompanied by the emission of large volume effusive products. Although studies on the Amazonian Craton are still scarce and controversial, the present study provides new evidence that this volcanism may have formed one of the largest Silicic Large Igneous Provinces (SLIP) on earth. Our data also confirm that at least two major Paleoproterozoic periods of formation of volcanic rocks exist in the Amazonian craton. This point is of great relevance for any future interpretation of the geological evolution of this craton.

1. Introduction

The Proterozoic Eon (2500–541 Ma) is the longest and youngest part of the Precambrian Supereon. This Eon represents the time just before the proliferation of oxygen accumulation and complex life on Earth. This period was likely the most tectonically active in Earth's history. In fact, it is also the period during which the largest portion of the modern crust (43%) and mineral ores were produced (Condie, 2000). Studies by Condie (2000) and Rino et al. (2004) suggest that crust production took place episodically, forming predominantly granitoidal crust and secondary volcanic and metamorphic rocks, some of which are extraordinarily well preserved.

The Amazonian Craton (AC) is one of the largest preserved Precambrian terrains in the world (4.6×10^6 km^2) (Almeida et al., 1981). It occupies approximately half of the Brazilian territory and it is the location of important mineral resources such as gold, iron, copper, and tin, among others (e.g. Faraco et al., 1997; Bahia and Quadros, 2000; Juliani, 2002; Klein et al., 2002, 2004; Reis et al., 2006; Monteiro et al., 2008; Juliani et al., 2014; Dall'Agnol et al., 2017). Although the

* Corresponding author at: YachayTech University, School of Geological Sciences and Engineering, Hacienda San José, Urcuquí, Ecuador.
E-mail address: matteoroverato1809@gmail.com (M. Roverato).

https://doi.org/10.1016/j.gr.2018.12.005
1342-937X/

geological investigation of the AC has recently seen a renewed interest of the national and international scientific community, mainly because of the massive presence of ore deposits, a general consensus related to the interpretation of its complex Paleoproterozoic evolution is still missing. Ancient volcanic regions represent a challenge for the understanding of emplacement dynamics especially when the stratigraphic relationships are difficult to decipher or blurred by erosion or vegetation cover. The present work constitutes the natural prosecution of previous investigations, carried out by our research group (Juliani et al., 2005, 2014; Juliani and Fernandes, 2010; Fernandes et al., 2011; Da Cruz et al., 2015; Roverato, 2016; Roverato et al., 2016, 2017), which are devoted to characterize the dynamics of emplacement of Precambrian volcanic rocks and their relationships to sedimentary facies. The study area comprises of the Tapajós Mineral Province (TMP) and the São Felix do Xingú (SFX) region, Pará state, northern Brazil. This contribution provides a means to interpret the volcanic processes active in this region during the Precambrian, mainly based on field observation and detailed lithofacies analyses. In addition, new geochemical and geochronological data are provided. Our study demonstrates how powerful is the approach of rock structure and texture characterization to the interpretation of the eruptive processes that governed the emplacement of volcanic and volcaniclastic sequences. The detailed lithofacies characterization and the stratigraphic reconstruction are important in this area and constitute a powerful key-tool to appropriately interpret the evolution of Precambrian volcano-sedimentary basins. Such an approach would turn to be useful when employed to investigate ancient terrains associated both to the ancient Amazonian felsic volcanism and Precambrian terrains in general.

2. Geological evolution of the southern portion of the Amazonian craton

The AC (Almeida et al., 1981) is located in the northern part of South America and is divided into two Precambrian shields, the Central-Brazil (or Guaporé, southern portion) and Guiana Shields (northern portion), which are separated by the Phanerozoic Amazonian Sedimentary Basin (Fig. 1) (Almeida et al., 1981). The entire craton has become tectonically stable before the end of the Precambrian (Dall'Agnol et al., 1994).

It has also been considered (Amaral, 1974; Hasui et al., 1993; Costa and Hasui, 1997) as a large Archean platform that had been reworked and reactivated during the ca. 2100 Ma Trans-Amazonian event. Alternative proposals based on geochronological and isotopic data (Teixeira et al., 1989; Tassinari and Macambira, 1999; Santos et al., 2000) divided the craton into several, predominantly NW-oriented, geochronological provinces, which have been interpreted as successive continental accretionary events, followed by granitic magmatism and tectonic reworking (Santos, 2003; Vasquez et al., 2008).

In a recent review Teixeira et al. (2019) report that the AC is the host of four LIP-scale (or SLIP) magmatic events discriminated by the Orocaima, Uatumã, Avanavero and Rincón del Tigre events. The igneous rocks described in the present manuscript are widely attributed to the Uatumã event (Dall'Agnol et al., 1999; Lamarão et al., 1999). The studied region is located between TMP and SFX, which is considered to be related to a continental arc, with a NE-SW arc migration as suggested by Juliani and Fernandes (2010), Fernandes et al. (2011) and Roverato et al. (2017). According to these authors a migration from the Serra do Cachimbo graben (in TMP where the subduction trench is located) toward the SFX could be explained by a change in the subducting angle of the oceanic plate beneath the continental plate. This is in agreement with the flat-subduction plate settings proposed by previous authors in other parts of the world (Ferrari et al., 2012; Gutscher et al., 2000; Kay et al., 2005; Mori et al., 2007; Manea et al., 2012).

2.1. The TMP (Tapajós Mineral Province)

The TMP (Fig. 2a) is primarily situated in the Tapajós–Parima geochronological/tectonic province (Santos et al., 2000) with the eastern part belonging to the Amazonia Central geochronological/tectonic

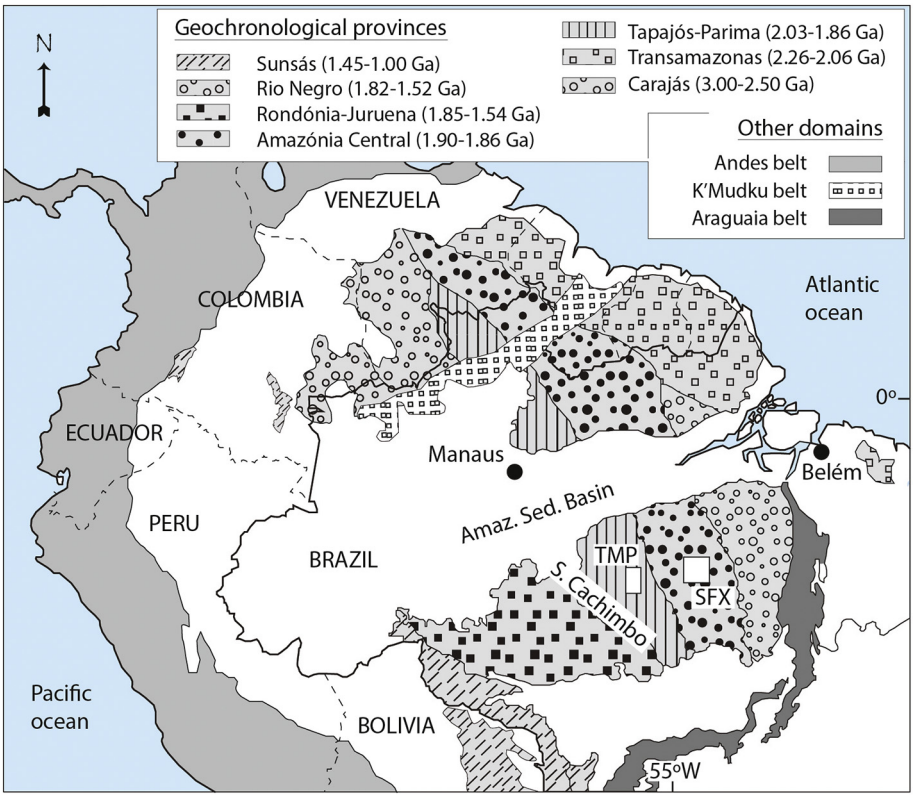

Fig. 1. Location map of the northern South America and the Amazonian Craton divided into several geochronological provinces and other domains according to Santos et al. (2000); TMP = Tapajós Mineral Province, SFX = São Felix do Xingú Region.

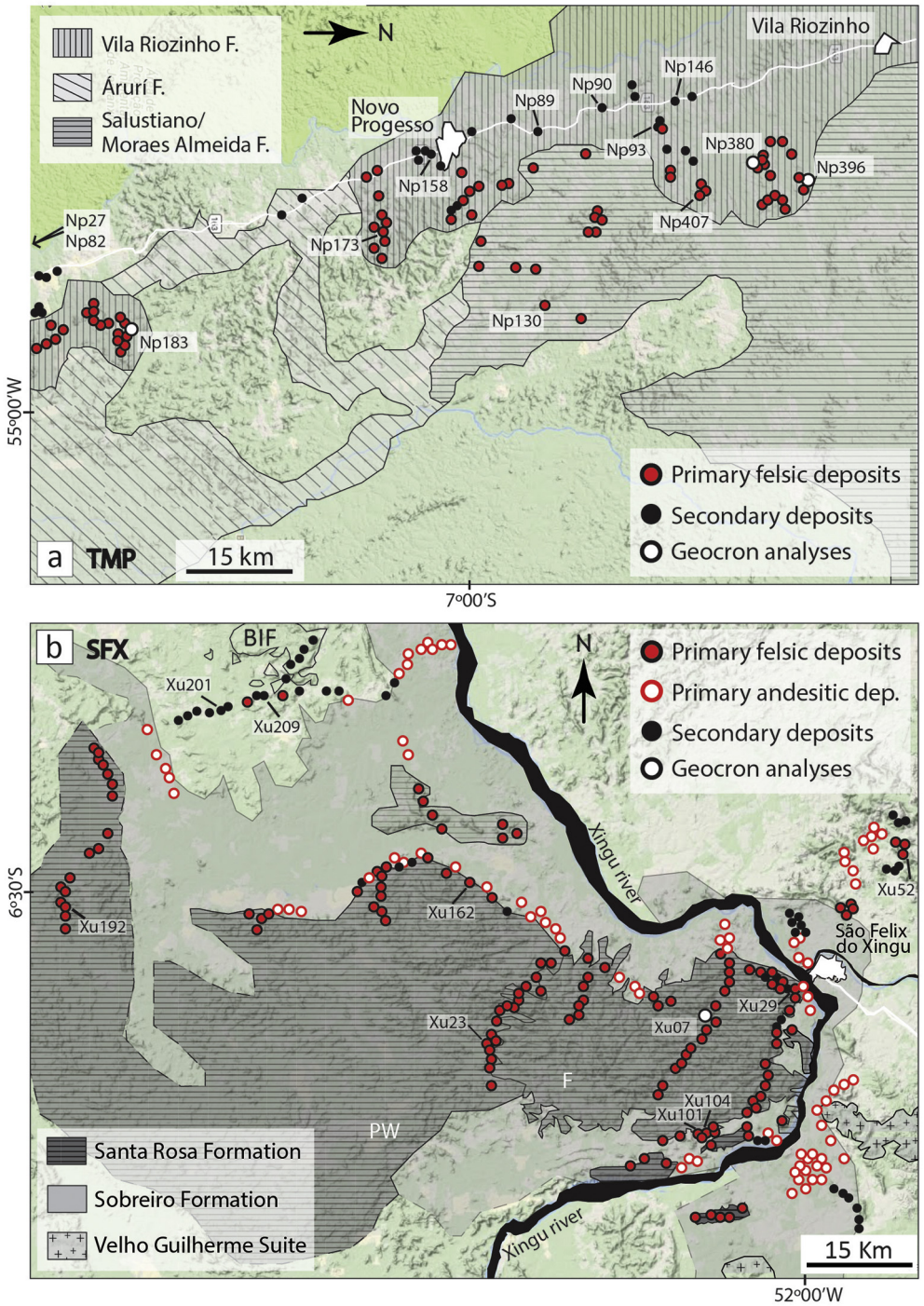

Fig. 2. Distribution map of the outcrops analyzed during the field campaigns in both regions a) Tapajós Mineral Province (TMP) and b) São Felix do Xingú region (SFX); PW = distribution of the Santa Rosa formation inferred during the present work; F = distribution of the Santa Rosa formation inferred by Fernandes et al. (2011); BIF = Banded Iron Formation; red and white dot refers to primary andesitic deposits analyzed in Roverato et al. (2017). In both figures are reported the outcrops described in the paper. (For interpretation of the references to color in this figure legend, the reader is referred to the web version of this article.)

province (Fig. 1). Based on Sm-Nd data and U-Pb ages (2100–1870 Ma), Santos et al. (2001, 2004) and Vasquez et al. (2008), identified several different domains for the Tapajós–Parima geochronological province and consider the TMP as a sequence of continental magmatic arcs (Ferreira et al., 2000; Santos et al., 2000, 2004; Vasquez et al., 2000; Klein et al., 2001; Lamarão et al., 1999, 2002). Late Paleoproterozoic volcanism of the Tapajós domain is represented by the Vila Riozinho Formation, formed by ca. 2000–1990 Ma intermediate to acid volcanic rocks (Lamarão et al., 2002), and by the Iriri Group that can be divided into the Bom Jardim (Almeida et al., 2000), Salustiano (1870 ± 0.008 Ma; Juliani et al., 2005) and Aruri (Pessoa et al., 1977) formations.

The Bom Jardim Formation (1898 ± 5 Ma, Santos et al., 2001) consists of mafic to intermediate high-K to shoshonitic calc-alkaline rocks while the latter formations are characterized by rhyolites, dacites and their pyroclastic and epiclastic derivatives. Juliani et al. (2005) considered the Bom Jardim volcanism as a preliminary step of the Iriri event representing pre-caldera volcanism followed by the Salustiano and Aruri caldera-related felsic activity. Post-caldera volcanism is characterized by ring-felsic volcanic structures that produced A-type (Vasquez

and Dreher, 2011) rhyolitic lavas and volcaniclastic deposits. Lamarão et al. (2002, 2005) described the felsic A-type Moraes Almeida volcanic sequence (1890 ± 6 Ma ryolite, 1875 ± 4 Ma ignimbite) represented by lavas and ignimbrites as part of the Iriri Group. Juliani et al. (2014) consider these last A-type rocks as similar in composition and age to the Santa Rosa Formation that crops out in the São Felix do Xingú region (SFX), which is considered to have formed by the same fissural-type volcanism (Juliani and Fernandes, 2010; Fernandes et al., 2011; Roverato et al., 2016). Preliminary data indicate that these rocks, for both TMP and SFX, display a very low grade of metamorphism, falling into the prehnite-pumpellyite field (Echeverri-Misas, 2010; Lagler et al., 2011; Fernandes et al., 2011).

2.2. The SFX (São Felix do Xingú region)

According to the work of Santos (2003) and Vasquez et al. (2008) the SFX region belongs to the Amazonia Central province (Fig. 1). The study area (Fig. 2b) is located near to São Felix do Xingú city, which corresponds to the southern portion of the Carajás Province. The Paleoproterozoic volcanic sequences in the SFX comprise the basal Sobreiro and upper Santa Rosa formations (Macambira and Vale, 1997; Juliani and Fernandes, 2010), which are crosscut by the Sn-bearing A-type granitoids of the Velho Guilherme Suite (Teixeira et al., 2002). Antonio et al. (2017) published the first U-Pb ages on zircons for the Santa Rosa Formation with 1877.4 ± 4.3 Ma for a rhyolite and 1895 ± 11 Ma for a dike. Recent geochronological data on a felsic porphyritic dike belonging to the Velho Guilherme suite yielded an age of 1857 ± 8.4 Ma (Shrimp U/Pb zircon analyses; Roverato, 2016). Other available geochronological data yielded ca. 1880 ± 6 Ma (TIMS Pb-Pb in zircon) for the Sobreiro Formation and ca. 1879 ± 2 Ma (TIMS Pb-Pb in zircon) for the Santa Rosa Formation (Fernandes et al., 2011; Pinho et al., 2006; Teixeira et al., 2002). Despite their similar ages, their geochemical compositions, geological features and eruption styles point to their non-cogeneticity (Fernandes et al., 2011). The Sobreiro Formation (SF) comprises basaltic andesite, andesite and less dacite massive lava flows and volcanoclastic rocks with high-K calk-alkaline signature (Fernandes et al., 2011; Roverato et al., 2017). According to Da Cruz et al. (2015) late- to post-magmatic hydrothermal alteration in these rocks is responsible for a secondary paragenesis characterized by epidote, chlorite, carbonate, clinozoisite, sericite, quartz, albite, hematite and pyrite. The Santa Rosa Formation (SRF) is described by Fernandes et al. (2011) as characterized by four lithological facies with A-type signature: (i) rhyolitic lava flow and thick dikes of banded rhyolite and ignimbrite; (ii) highly rheomorphic felsic ignimbrite associated with un-welded ash tuff; (iii) felsic crystal tuff, lapilli-tuff and co-ignimbritic breccias; (iv) granitic porphyry stocks and dikes and subordinate equigranular granitic intrusions.

3. Lithofacies analyses

Lithofaciological analyses were carried out in the course of this study in order to understand the geodynamic evolution of the study area. Here we report on the lithofacies analysis of rocks recognized during our field campaigns (and after in petrological thin section) at the TMP and SFX provinces. Within the study area (TMP and SFX), massive to banded lava flows and rheomorphic ignimbrites (Fig. 3) as well as felsic volcaniclastic rocks of various origin (Figs. 4–8, 11) are frequently found. Reworked (secondary) volcaniclastic rocks (Figs. 9, 10) and sedimentary alluvial/coastal clastic deposits (epiclastic) are also widely distributed in both TMP and SFX areas. Primary volcaniclastic rocks are here defined as those fragmental products formed during a syn-eruptive explosion, which were deposited regardless of whether their transport occurs through air, water, granular debris or a combination of them (McPhie et al., 1993; White and Houghton, 2006; Manville et al., 2009; Roverato et al., 2017). On the other hand, all the units deposited as a consequence of a reworking process of pre-existing volcanic units are defined here as secondary volcaniclastic rocks. We also introduce into this group all those epiclatic products that constitute sediments that had been reworked before, independent of their source and composition. Table 1 shows a description and interpretation of the volcaniclastic lithofacies, both primary and secondary, for the deposits identified in the study areas.

4. Lava flows and rheo-ignimbrites

As already discussed by Roverato et al. (2016), the absence of unequivocal vitroclastic textures complicates the distinction between volcaniclastic and layered lava flows in general and, more in particular, for the ancient volcanic rocks investigated here. Lava flows found in the TMP and SFX provinces have both massive and banded structures (Fig. 3) while still maintaining, in some cases, glassy (obsidian) and aphanitic to porfiritic texture. Their composition varies from trachytic to rhyolitic with various content of alkalies (see Section 8). The phenocryst assemblage consists mainly of plagioclase, quartz, Fe-Ti oxides and accessory-amount of zircon and apatite. Plagioclase and bipiramidal quartz crystals (Fig. 3a), with a maximum size of 3–4 mm, range from euhedral to anhedral, showing moderate to intense resorption. Plagioclase shows sieve texture indicating non-equilibrium conditions likely determined by magmatic transport. K-feldspar is also present as anhedral crystals in the groundmass often associated with sericite as alteration phase. Samples are generally affected by variable intensity of hydrothermal alteration. Plagioclase phenocrysts, in particular, present diffuse potassic and minor propylictic alterations. Abundant spherulites and lithophysaes of variable size, from millimetric to decimetric, were recognized in almost every sample and are thus common in these rocks (Fig. 3b, c). The spherulites (radiating fibers of K-feldspar and cristobalite), ranging from few millimeters to 2 cm, are typically associated with perlitic fractures. Their content can vary from 10 vol% to 70% in the investigated rocks. A large amount of the spherulites developed into lithophysae commonly reaching 10–12 cm as a consequence of cooling and degassing processes. In the obsidian-type lavas (Fig. 3c), the groundmass is characterized by a micro-granophiric-like devitrification texture characterized by crystallization of amorphous quartz and alkali feldspar, a process that occurred after the emplacement of lava bodies. Several rocks show textures that are not easy to be associated to either lava flows or flows of fragmented material which underwent rheomorphism (Fig. 3d–g). Both banded lavas and rheo-ignimbrites display folds (Fig. 3d–g, see also Fig. 11e) and sub-parallel bands on mm- to dm-scale, planar to wavy (Fig. 3e, see also Figs. 6 and 7) (parataxitic fabric), that deform and flattened around lithic fragments and crystals which alignment suggests the flow direction. In thin sections, the bands are characterized by extremely flattened vitroclastic textures with the former glass completely replaced by a mixture of quartz and feldspar (Roverato et al., 2016).

5. Primary volcaniclastic rocks

We consider primary volcaniclastic rocks those dense, scoriaceous and pumiceous products of fragmental character emplaced by explosive processes. With pyroclastic we refer to fragmental material generated by any kind of explosive volcanic activity and transported as ash-fall and pyroclastic density currents (Manville et al., 2009), which deposition occurs by suspension settling, from traction, by en masse freezing, or any combination of these (White and Houghton, 2006). Depending on the mechanism of transport and the eruptive style these clastic rocks were distinguished into two different categories, i.e. massive and stratified; and they can vary from well sorted, poorly sorted or unsorted. The rocks are predominantly rhyolitic in composition (Fernandes et al., 2011; Roverato et al., 2016) and there is no significant geochemical difference from the lava flows. Nine main lithofacies (Lf) have been recognized for the volcaniclastic rocks: six of them are massive and three are stratified.

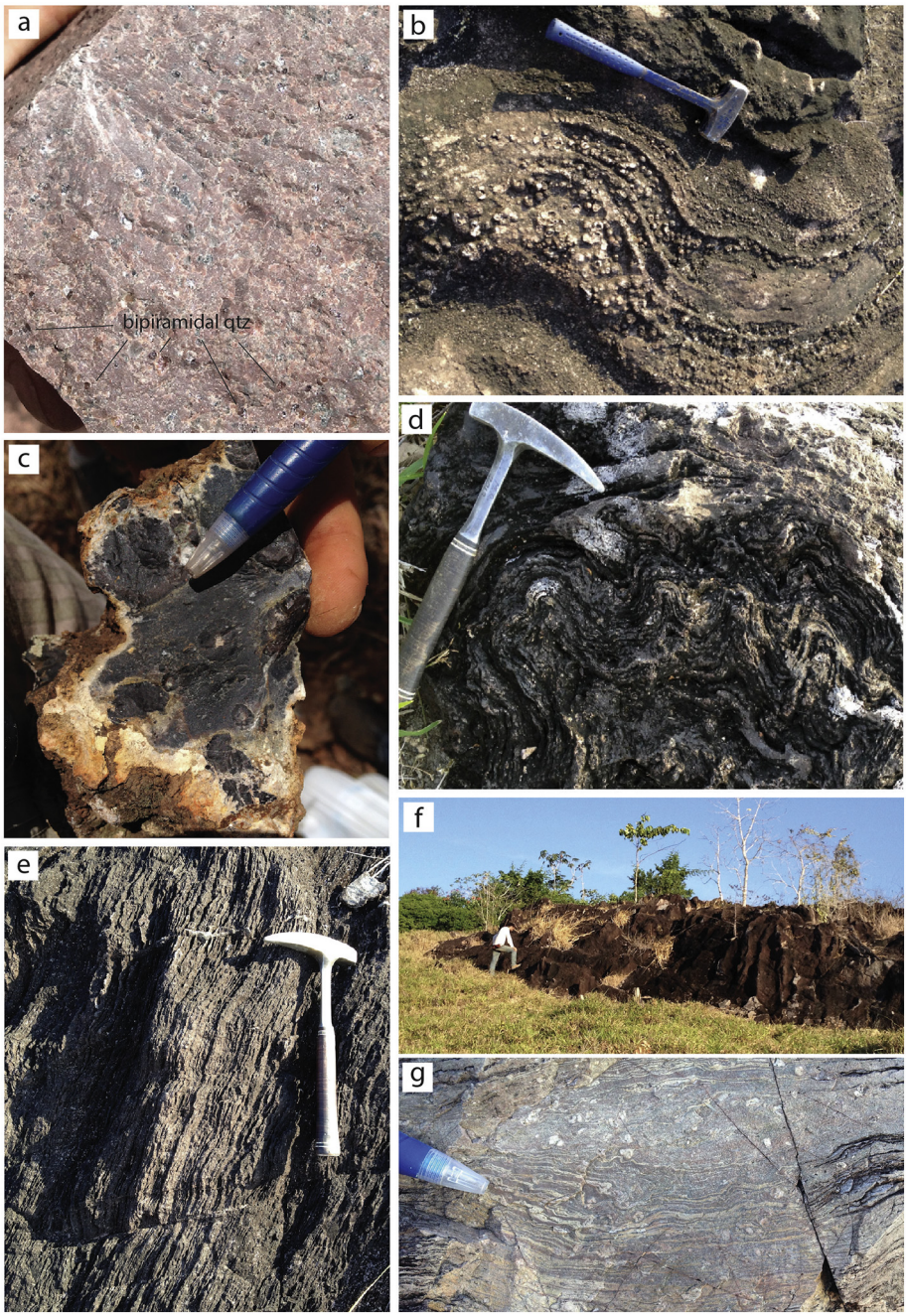

Fig. 3. Massive and banded lavas and rheo-ignimbrite (?) deposits. a) Np173 (7°33′52.31″ S, 55°10′58.80″ W), b) Xu23 (6°41′08.65″ S, 52°25′55.67″ W), c) Xu101 (6°52′12.82″ S, 52°09′16.12″ W), d) Xu52 (6°28′19.32″ S, 51°50′08.90″ W), e), f), g) Np396 (6°32′41.06″ S, 55°23′59.37″ W); see Fig. 2 for the outcrops location. For the lithofacies description and more details see the text.

5.1. Massive

Six massive lithofacies (mAL, mLA, mLB, *l*-gwLA, *m*-gwLA and *h*-gwLA) were recognized during our field campaign, three of them belong to the welded ignimbrites sub-group (Table 1). By using the granulometric classification proposed by Fisher (1961), ash is defined as any fragment with size <2 mm, lapilli are fragments with size between 2 and 64 mm and blocks (or bombs) have sizes >64 mm. Massive lithofacies includes all those deposits that display a massive coherent structure. Outcrops of such kind of lithofacies are constituted by a high percentage of ash up to block-rich textures. Most of the observed samples appear to have been affected by devitrification processes of the juvenile pyroclastic fragments and matrix. The presence of juvenile material linked with other observed textures such as broken crystals (Best and Christiansen, 1997) and eutaxitic fabric allows us to confirm that the rocks belonging to lithofacies mAL, mLA, *l*-gwLA, *m*-gwLA and *h*-gwLA are fragmental and pyroclastic in origin. We discuss the meaning of Lf mLB below in Section 5.1.2.

5.1.1. Lf mAL; mLA (massive Ash to Lapilli; massive Lapilli and Ash)

Description: the ash to lapilli (mAL) and lapilli *and* ash (mLA) deposits (Figs. 4a–e, 6) are heterolithologic, matrix supported, containing angular to sub-rounded medium to coarse devitrified lapilli (displaying axiolitic fabric), banded fragments, occasional (or absent) lithics and angular-shaped broken crystals of plagioclase, bipiramidal quartz and rare oxides (Fig. 5). In mLA, clasts <25 cm in size are randomly immersed in the groundmass (Figs. 4d and e, 11d). Some of them are altered by carbonate minerals. Groundmass of mAL and mLA is formed

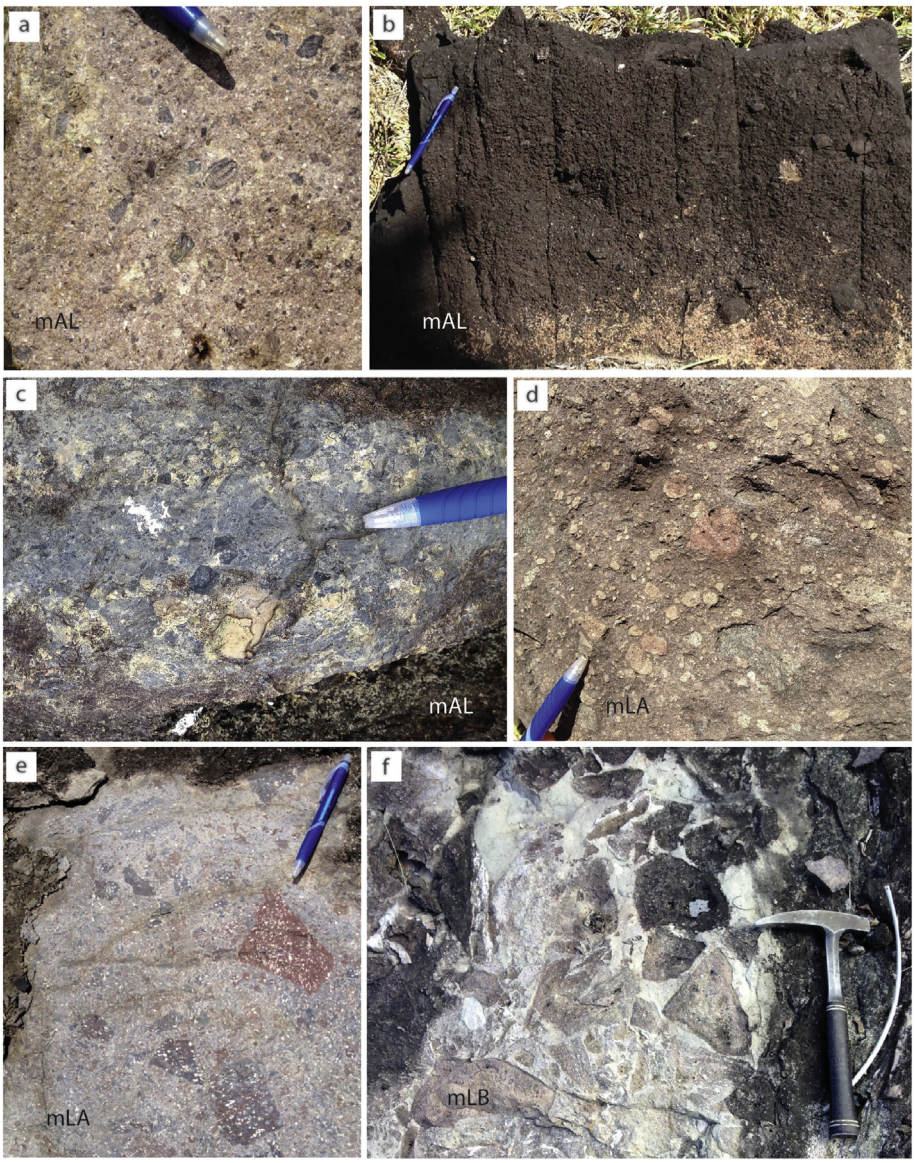

Fig. 4. Massive primary volcaniclastic rocks with different proportion of ash, lapilli and blocks. All the deposits are interpreted to be emplaced from pyroclastic density currents except (f) that is interpreted as a basal-breccia of a lava body. a) Xu104 (6°52′22.96″ S, 52°08′15.91″ W), b) Np183 (7°32′04.13″ S, 55°08′50.02″ W), c) Np93 (6°44′16.60″ S, 55°27′12.96″ W), d) Xu29 (6°41′42.51″ S, 52°01′23.06″ W), e) Xu07 (6°41′56.36″ S, 52°08′42.27″ W) f) Xu192 (6°31′31.92″ S, 53°02′36.60″ W); see Fig. 2 for the outcrops location. For the lithofacies description see the text and Table 1.

by K-feldspar and quartz crystals, devitrified ash fragments and sericite crystals as phase of alteration (Fig. 5).

Interpretation: the general massive aspect and the poor sorting of mAL and mLA point to a laminar granular flow transport regime and the fine content suggests the deposition from a dilute fluid escape-dominated flow-boundary zone in which turbulent shear-induced tractional segregation is suppressed (Branney and Kokelaar, 2002; Sulpizio et al., 2007; Roverato et al., 2017). These lithofacies are interpreted as ash flow deposits suggesting the deposition from a pyroclastic density current (PDC) (Lenhardt et al., 2011; Sulpizio et al., 2014; Roverato et al., 2017). The coarser lithofacies mLA (Fig. 4e) could be related to proximal co-ignimbritic breccias as result of deposition by denser pyroclastic granular flows (Branney and Kokelaar, 2002). The angular aspect of the clasts indicates short-period transport.

5.1.2. Lf mLB (massive Lapilli and Block)

Description: this lithofacies (Figs. 4f, 7) represents monolithologic coarse-grained rocks having high-clast content (clast:matrix ratios up to 3:1). Angular/sub-angular coarse lapilli and blocks up to 50–60 cm of devitrified banded or massive lava fragments are immersed in a devitrified fine lapilli and coarse ash matrix.

Interpretation: the blocky and monolithologic coarse-grained aspect of the lithofacies mLB and its position underneath thick flow-deposits is attributed to the basal auto-brecciation of lava flows and/or rheo-ignimbrite flows. Despite the lithofacies is likely a consequence of an effusive volcanic activity (in the lava-flow case) it is considered anyway as part of the volcaniclastic group due to its fragmental character.

5.1.3. Lf l-gwLA; m-gwLA; h-gwLA (welded Ignimbrites)

Description: all massive deposits displaying welding characteristics have been grouped in the "welded ignimbrites" group (Table 1), following the idea of "grade of welding" (Walker, 1983) (i.e. the amount of welding and compaction exhibited by deposits). The rocks are matrix-supported with sub-rounded to angular lapilli and ash lithic clasts, euhedral, subhedral and broken crystals (plagioclase and less quartz) and deformed devitrified juvenile fragments (*fiamme*). Slightly- (low-grade, *l*-gwLA), medium- (medium-grade, *m*-gwLA), well-stretched (high-grade, *h*-gwLA) *fiamme* (Fig. 6), as well as, devitrified shards

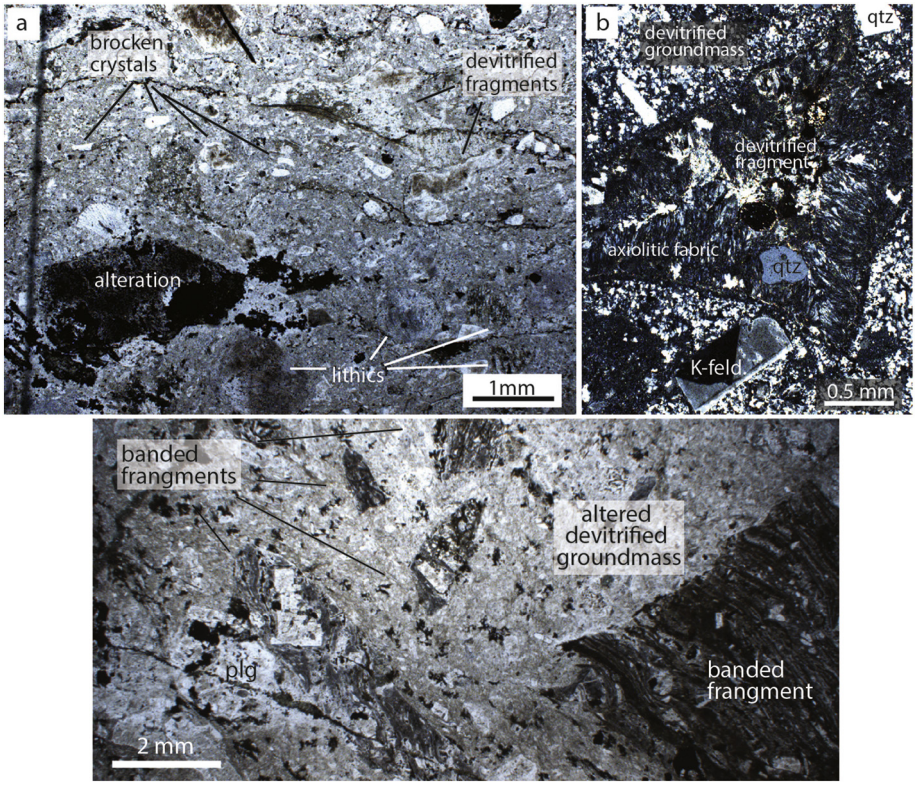

Fig. 5. Microphotographs of different massive ash and lapilli ignimbrite deposits in thin section: a) broken crystals suggesting the fragmental character of the rock; b) detail of a devitrified juvenile fragment displaying axiolitic fabric; c) banded sub-millimetric to millimetric lithic fragments immersed in a devitrified groundmass.

define the eutaxitic fabric (Roverato et al., 2016). These fragments varying from millimetric to 3–4 cm in size are immersed in a homogeneous micro-granophiric-like devitrified groundmass (see Roverato et al., 2016 for details). Fig. 6 shows a stratigraphic column representing a 35 m thick sequence of ignimbrite deposits found in the TMP, displaying very low-grade to high-grade welded fabric where the grade of welding increases toward the top of the succession. The very top of the sequence is characterized by columnar jointing.

Interpretation: the massive aspect and the poor sorting of the lithofacies *l*-gwLA, *m*-gwLA and *h*-gwLA point to a laminar granular flow transport regime, interpreted to be deposited from a pyroclastic density current (PDC). The welded character of these lithofacies is indicative of hot PDC emplacement and compaction that result into the low- up to high-grade eutaxitic fabric. This process is favored by loading-compaction, low-viscosity fragments, high temperature (i.e. >900 °C), cooling of gas-permeable fragments (pumices) and dissolved water (Branney and Kokelaar, 2002; Roverato et al., 2016 and references therein).

5.2. Stratified

These lithofacies, although commonly associated with ignimbrites, are not very spread in the studied areas. We also didn't find any alternation between massive and stratified deposits even if this association is a common occurrence in PDC deposits (Sulpizio et al., 2014; Roverato et al., 2017), alternating dilute (stratified deposits resulting) and concentrated (massive deposits resulting) regimes during transport (Sulpizio et al., 2014). Just one example has been found in TMP and is reported in the stratigraphic reconstruction of Fig. 11.

5.2.1. Lf sA; xsA; dsAL (stratified Ash; cross-stratified Ash; diffusely stratified Ash to lapilli)

5.2.1.1. Description. The stratified samples and outcrops analyzed comprise well sorted very fine to fine ash organized in millimetric to sub-millimetric parallel (sA) or cross-stratified (xsA) layers, with sharp or gradational changes in grain size (Fig. 8). The fragments are represented by devitrified shards, crystals (plagioclase), and rare (or absent) lithics (Fig. 8d) immersed in a devitrified groundmass. Diffuse-stratified lithofacies dsAL display a coarser character with coarse lithic and devitrified ash and lapilli fragments forming well developed parallel continuous meter-long stratification (or very-low angle cross-stratification) at centimeter scale (Fig. 11b), with gradational changes in grain-size. The sorting varies from well to moderate.

5.2.1.2. Interpretation. The fine parallel layering of shards material displayed by lithofacies sA is interpreted here as being deposited under the product of sedimentation by the upper and highly dilute ash-cloud that accompany a pyroclastic-density current. We don't exclude the direct sedimentation from tephra fall-out activity. Cross-stratified (Lf xsA) and diffuse-stratified (Lf dsAL) deposits indicate tractive processes usually attribute to pyroclastic surge-type depositional condition from dilute currents (Cas and Wright, 1987; Lenhardt et al., 2011; Roverato et al., 2017). We interpreted these as pyroclastic surge deposits although Lf dsAL could also be the product of coarse ash fall-out processes. Pyroclastic surge deposits usually display small volume and rarely reach >10 km from their source (Lenhardt et al., 2011). Conversely, fall-out deposits could emplace tens of kilometers from their source.

6. Secondary volcaniclastic/epiclastic rocks

The nomenclature of Fisher (1961) is applied also for the secondary volcaniclastic rocks as follow: silt (2<>64 μm), sand (64 μm<>2 mm), gravel (2<>64 mm), cobble (64<>256 mm). These rocks are considered as the product of reworking and erosive processes. The clasts belonging to this group show a wide range of composition, size and shape variations. Based on their component, texture and fabric, we recognized

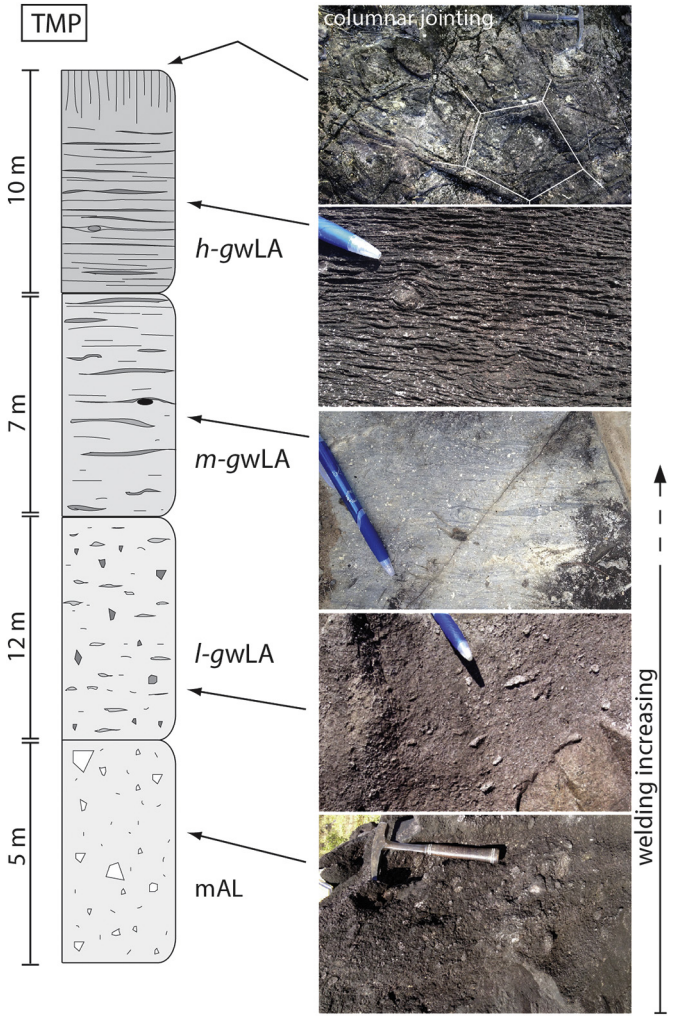

Fig. 6. Reconstructed schematic stratigraphic column and associated photographs representing the evolution of ignimbrite deposits cropping out in the TMP (Np183; 7°32′04.13″ S, 55°08′50.02″ W); note the increase of welding from the base to the top.

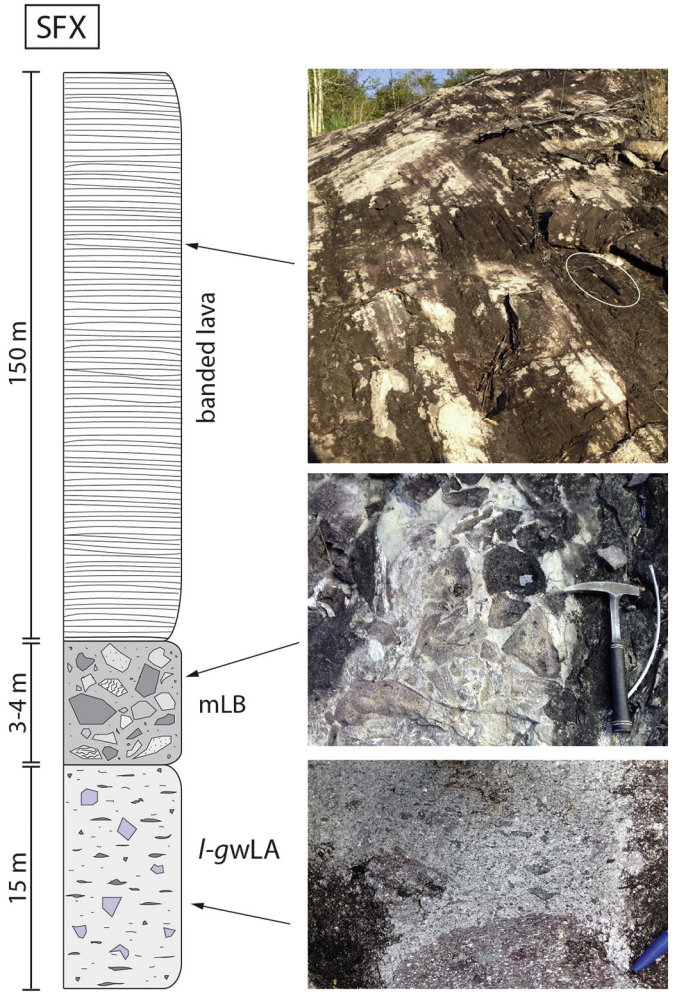

Fig. 7. Schematic stratigraphic column and relative photographs of a >150 m thick felsic banded lava(s) cropping out in SFX (Xu192; 6°31′31.92″ S, 53°02′36.60″ W) overlying a basal breccia (Lf mLB) and an ignimbrite deposit characterized by a low grade of welding (Lf *l-gw*LA).

five massive, both matrix- and clast-supported, and four stratified lithofacies (Fig. 9).

6.1. Massive

6.1.1. Lf mS (massive Sand)

6.1.1.1. Description. This lithofacies consists of reddish moderately to well-sorted, massive, fine- to medium grained sand forming parallel strata intercalated to clast-supported conglomerate deposits (Lf csG) (Fig. 9a). The sandstone strata extend tens of meters and present thinness between 0.4 and 0.8 m. Lf mS is predominantly composed of quartz, feldspar and minor rock fragments. Contacts between mS and csG are sharp with rare slightly erosional surfaces. The tops of the sandstone are characterized by the presence of centimeters ripples (Fig. 9b).

6.1.1.2. Interpretation. The massive sand (mS) and the small ripples found at the top of the strata indicate low energy under tractional currents in shallow water conditions (Collinson and Thompson, 1982; Lenhardt et al., 2011). The alternation of Lf csG and mS indicates changes in energy conditions of sedimentation. We interpret these oscillations as belonging to a subaqueous-subaerial fan-delta interface setting where continental supply of material alternates to under-water sand accumulation (Lf mS).

6.1.2. Lf csG (clast supported Gravel)

6.1.2.1. Description. This lithofacies (Fig. 9a, c, d) is massive, clast to matrix supported, with heterolithologic felsic rounded high-spherical coarse gravel with a sandy inter-clast matrix. Clasts are mainly characterized by massive and banded medium- to coarse-size felsic lava fragments (and rare quartz; size does not exceed 5 cm) and present rounded with low- to high-sphericity. We found lithofacies csG also associated to xsSG (see below Section 6.2.2) (Figs. 9c, 10b).

6.1.2.2. Interpretation. Lithofacies csG is dominated by water flow processes where matrix plays a secondary role. The clast-supported character and less matrix content indicates that water removed the finer particles during transport and deposition. Lf csG display rounded clasts and well-sorting indicative of good selection during transport and emplacement. The rounded character of csG and the presence of matrix in the deposits suggest a laminar debris-flow regime in medial reaches of stream-dominated fluvial/alluvial fans (Mueller and Concoran, 1998).

6.1.3. Lf csGS (clast supported Gravel to Sand)

6.1.3.1. Description. Lf csGS (Figs. 9e, 11c) is massive, moderately well-sorted and clast-supported. Clasts (gravel to sand) present sub-rounded to sub-angular with low/medium sphericity with maximum

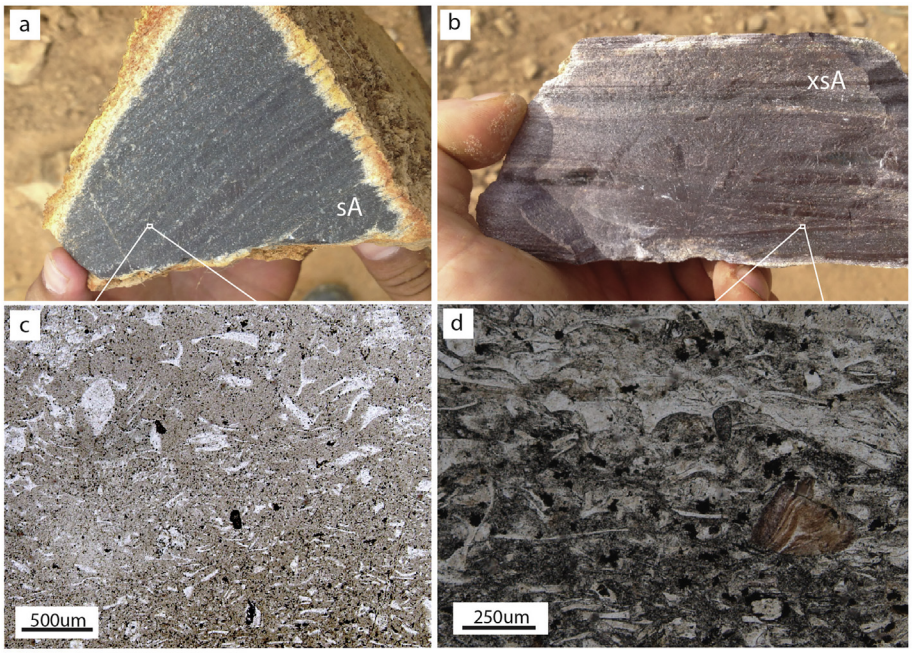

Fig. 8. Stratified primary volcaniclastic rocks, a) related to sedimentation by highly dilute ash-cloud (Np130; 6°54′16.09″ S, 55°10′59.38″ W) and, b) attribute to pyroclastic surge-type depositional condition from dilute currents (XU162; 6°32′28.39″ S, 52°25′26.07″ W); see Fig. 2 for the outcrops location. Relative thin section microphotographs (c/d) showing micrometric shards. For the lithofacies description see the text and Table 1.

size of 2–3 cm. The rocks belonging to this lithofacies are mainly formed by massive felsic lava fragments with different color and crystallinity.

6.1.3.2. Interpretation. Lf csGS is dominated by water flow processes where matrix plays a secondary role. The clast-supported character and less matrix content indicates that water removed the finer particles during transport and deposition. This lithofacies represents deposition within a debris-flow dominated fluvial/alluvial environment. Poor sorting, clast-supported and sub-angular clasts point to deposition by localized laminar hyperconcetrated-flows in volcanic fans fringing flanks of volcanic edifices. Single cross-beds are usually ca. 1 cm thick.

6.1.4. Lf csGC (clast supported Gravel and Cobble)

6.1.4.1. Description. Lithofacies csGC (Fig. 9f) is massive, low-sorted and clast-supported. The clast population is characterized by sub-rounded, low/medium sphericity, massive felsic porfiritic fragments with maximum size up to 20 cm. This lithofacies has an interstitial matrix characterized by medium to coarse sand.

6.1.4.2. Interpretation. Lf csGC is dominated by water flow processes where matrix plays a secondary role. The clast-supported character and less matrix content indicates that water removed the finer particles during transport and deposition. This lithofacies represents deposition within a debris-flow dominated alluvial environment. Poor sorting, clast-supported and sub-angular clasts likely points to deposition by localized non-cohesive debris-flows.

6.2. Stratified

6.2.1. Lf xsS (cross-stratified Sand)

6.2.1.1. Description. Lithofacies cross-stratified Sand (Fig. 10a) consist of white to brownish low-angle cross-stratified coarse quartzitic sandstone. The sandstones are characterized by lobe to sheet-shaped bodies. Major bedsets are recognized ranging in thickness from 0.5 to 1.5 m, composed of fine-grained sandstone dominated by medium-angle cross strata (18–20°). Single cross-beds are usually 0.7–1 cm thick. The outcrops displaying this lithofacies extend tens of meters with sharp upper and lower contact.

6.2.1.2. Interpretation. The cross-stratification of xsS is interpreted as formed in fluvial channels attesting the deposition from crested dune bed-forms that formed under condition of lower flow regime (Collinson, 1966; Miall, 1996; Capuzzo and Wetzel, 2004; Went, 2016). The deposition of medium-angle cross-bedding within large-scale examples of beds indicates that these larger beds are likely a product of bar migration. The beds are interpreted as channel-fill deposits (Lenhardt et al., 2017) related to a fluvial environment likely associated to meandering or braided rivers. Shoreline deposition developed around margins of immature marine basins is also considered.

6.2.2. Lf xsSG (cross-stratified Sand and Gravel)

6.2.2.1. Description. Lf xsSG (Fig. 10b) is characterized by crystal-lithic fine to coarse sand and fine gravel (max 5–6 mm in size) organized in cross-bedded stratification. Clasts display medium roundness and sphericity and are mostly composed by felsic fragments. Stratification is defined by alternating of well to poorly sorted, fine to coarse millimeters-thick strata. The finer black layers are formed by sub-millimetric hematite sand.

6.2.2.2. Interpretation. Lf xsSG correspond to cross-stratified water reworked deposits. The cross-stratified thicker fine gravelly strata, alternated with sandy layers laterally discontinuous, were interpreted as different pulses as the result of rapid deposition from hyperconcentrated flows (Zanchetta et al., 2004) in a stream-dominated fluvial/alluvial setting. Alternation with csG (Fig. 9c) represents difference of energy condition.

6.2.3. Lf dsSt (diffusely layered Silt)

6.2.3.1. Description. This lithofacies consists of parallel, lenticular, truncated, and locally low-angle cross-stratified multicolor millimetric well-sorted fine- to very fine-grained sand and silt strata (Fig. 10c). Within the sandy bedset, a thinning- and fining-upward trend may be

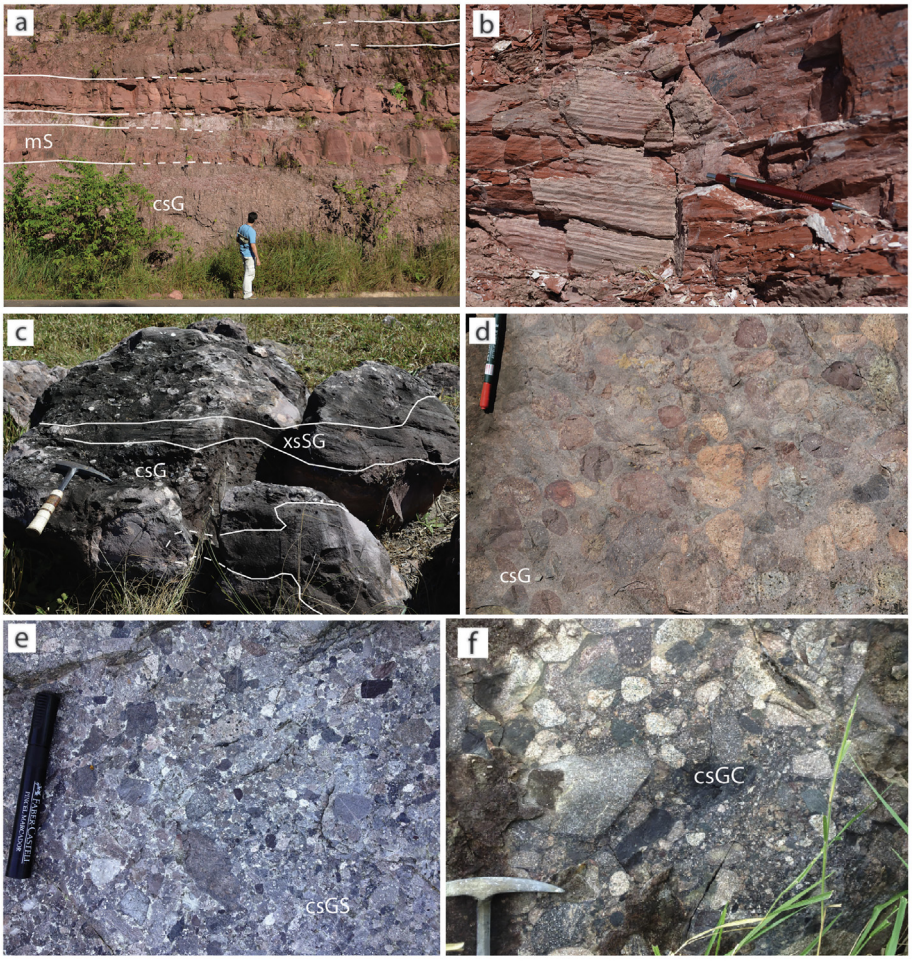

Fig. 9. Massive sedimentary rocks. a) The alternation of lithofacies *csG* and *mS* indicates changes in energy conditions of sedimentation belonging to a subaqueous-subaerial fan-delta interface (Np146; 6°42′58.24″ S, 55°28′53.49″ W); b) detail of centimeters ripples of Lf *mS* (Np89; 6°54′39.36″ S, 55°26′12.28 W); c) Lf *csG* is also associated to Lf *xsSG* (see stratified rocks in Section 6.2) (Np27; 8°08′18.43″ S, 54°54′37.33″ W). d) Np27, e) Xu209 (6°13′55.26″ S, 52°42′29.25″ W), f) Np158 (7°03′33.79″ S, 55°24′11.84″ W); the rounded and clast supported character of these lithofacies is linked with fluvial/alluvial deposition by debris-flow dominated processes; see Fig. 2 for the outcrops location. For a more detailed lithofacies description see the text and Table 1.

distinguished. Small and straight groove marks have been detected and reduced tiny slump folding is also presence in some parts.

6.2.3.2. Interpretation. Lithofacies dsSt displays diffuse fine stratification with tiny ripples, suggesting transport and sedimentation in shallow water. The thin sheet-shaped is interpreted as flood sediments (Lenhardt et al., 2011). These deposits are interpreted to have been formed in low energy lacustrine environment or ponds (Collinson, 1966; Roverato et al., 2017) characterized by small turbidities successions affected by scouring and tiny deformations (slumps) of the sediments.

6.2.4. Lf bChS (bedded Chert and Sand)

6.2.4.1. Description. The bedded chert lithofacies (with sand) (bChS) (Fig. 10d) crops out in both regions and it is characterized by outcrops that can be traced on strike for hundreds of meters. The facies consist of thin laminated pinkish chert (layers <1 mm in thickness) with darker laminae intercalated, formed predominantly by hematite (Lenhardt et al., 2017). The layers are composed by microcrystalline quartz. In some portions, these lithofacies are associated with fine to medium sand composed mainly by quartz and less volcanic fragments.

6.2.4.2. Interpretation. This lithofacies is interpreted as inorganic precipitation of silica in a closed lake basin mainly due to its association with volcanic rocks and fine sandstone (Blatt et al., 1980; Eriksson et al., 1994). The picture in Fig. 10d shows elongated ripped-up millimetric fragments of chert immersed in the sandstone eroded by low-energy stream flow or local lacustrine turbidites. As suggests by Lenhardt et al. (2017) the chert may have formed during repeated pulses of hydrothermal fluids that circulated into the lake water during hiatuses in the volcanism (Van Kranendonk, 2006).

7. Analytical methods for geochemistry and geochronology

A total of 19 new samples (9 volcaniclastics and 10 lava flows) from the Tapajós region (associated with the data published in Roverato et al., 2016; Table 2) were analyzed for bulk rock major and trace elements. Major element bulk rock analyses were performed by X-ray fluorescence, using a wavelength dispersive Philips PW 2400 spectrometry, using fused glass disks according to procedures described by Mori et al. (1999). Accuracy was >2%. Trace element analyses in selected samples were performed by Inductively Coupled Plasma-Mass Spectrometry (ICP-MS) using the procedure described by Navarro et al. (2008). Accuracy, determined with respect to the reference standards BHVO-2 and BR, was 0.5–2%.

Zircon grains were examined with a FEI-QUANTA 250 scanning electron microscope equipped with secondary-electron and cathodoluminescence (CL) detectors at the Instituto de Geociências - Centro de Pesquisas Geocronologicas - Universidade de São Paulo (IGc-CPGeo-USP); the most common conditions used in CL analysis

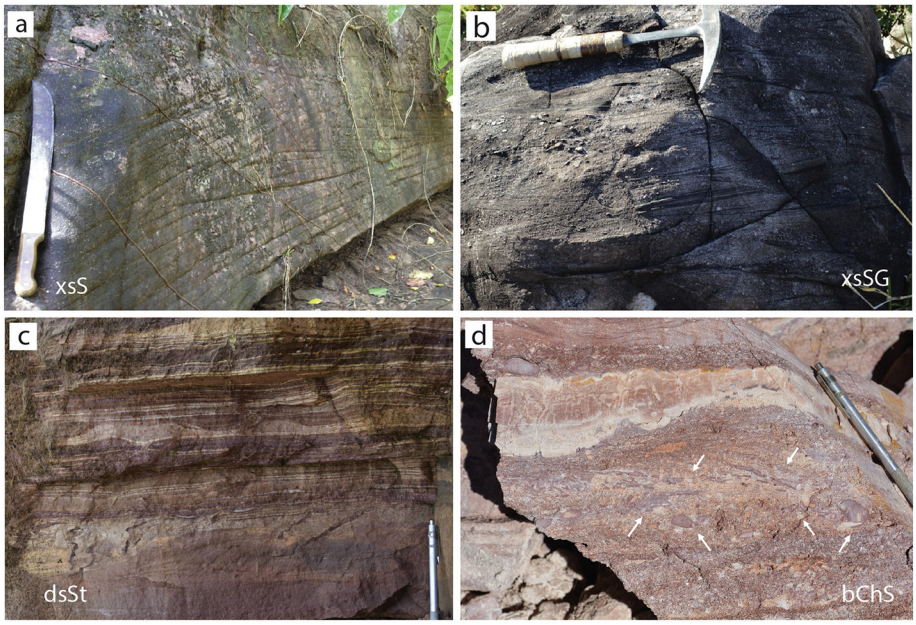

Fig. 10. Stratified sedimentary rocks. a) The quartzitic sandy cross-bedded lithofacies is interpreted as formed in fluvial channel or around margins of immature marine basins (?) (Xu 201; 6°16′12.95″ S, 52°52′18.84″ W); b) the cross-stratified water reworked lithofacies is linked with stream-dominated fluvial/alluvial settings (Np82; 8°03′40.79″ S, 54°50′43.52″ W); c) the silty sedimentation likely belong to a lacustrine environment characterized by small turbidities (Np158; 7°03′33.79″ S, 55°24′11.84″ W); d) the top of the photographs shows the Lf *bChs* interpreted as inorganic precipitation of silica (chert) in a closed lake basin; white arrows show fragments of the chert deposit eroded by low-energy sandy stream flows or local lacustrine turbidites (Np90; 6°49′50.20″ S, 55°28′15.47″ W); see Fig. 2 for the outcrops location. For a more detailed lithofacies description see the text and Table 1.

were 60 μA of emission current, 15.0 kV of accelerating voltage, 7 μm of beam diameter, 200 μs of acquisition time, and a resolution of 2048 × 1887 pixels and 345 dpi. Selected samples were analyzed for U-Pb isotopes using a SHRIMP-IIe also at IGc-CPGeo-USP, following the analytical procedures of Williams (1998) as reported by Giovanardi et al. (2015). Correction for common Pb is based on the measured ^{204}Pb, and the typical error for the $^{206}Pb/^{238}U$ ratio is <2%; U abundance and U-Pb ratios were calibrated against the TEMORA-II standard. The dataset consists of 56 new U-Pb SHRIMP-II analyses and is reported in the supplementary material. Thirty-five analyses were performed on zircon grains from the Tapajós region as follow: 11 analyses on sample NP380-C, 11 analyses on sample NP183 and 13 analyses on sample NP396-B. Eleven analyses were performed on zircon grains from Xingú sample XU08. For all samples, $^{207}Pb/^{235}U$ and $^{206}Pb/^{238}U$ concordia ages (with 95% of confidence level and 2σ error) are calculated using Isoplot 4.1 software (Ludwig, 2009).

8. Geochemistry of the TMP samples

Independently of their nature (lavas or volcaniclastic), the rocks of the TMP follow a typical calc-alkaline trend (Fig. 12). They are mostly rhyolitic in composition (Table 2), with four exceptions which fall in the trachytic field. In addition, their low LOI values (0.32–3.51%) and the low FeO content (0.78–3.26%) together with the negative correlation FeO vs SiO_2 appears to indicate that the investigated volcanic rocks neither underwent significant alteration processes nor they belong to sedimentary suites which commonly contain water rich clay minerals. TMP volcaniclastic and lava flows show similar negative correlation between TiO_2, Al_2O_3, MgO, FeOt, CaO, Na_2O and P_2O_5 with SiO_2. A negative correlation between K_2O and SiO_2 also exists for the volcanoclastic, but not for the lava flows. The similar trends observed suggest that both these kind of rocks are originated by similar magmatic sources. Such a conclusion is supported by similar variation paths, although with different values, of minor and trace elements (Fig. 13). In particular, TMP lava flows show LREE enrichment ($(La/Yb)_N$ = 10.68–21.45; normalization to Chrondrite I from Anders and Ebihara, 1982) and a negative Eu anomaly which increases from trachytes ($(Eu/Eu^*)_N$ = 0.89–0.78) to rhyolites ($(Eu/Eu^*)_N$ = 0.69–0.31) (Fig. 13). The Eu negative anomaly, shown from all the samples, is expression of feldspar fractionation. On the other hand, volcaniclastics rocks show similar LREE enrichment ($(La/Yb)_N$ = 11.12–28.10) and negative Eu anomaly ($(Eu/Eu^*)_N$ = 0.97–0.37) (Fig. 13). In addition, volcaniclastics have higher LREE abundances with respect to lavas (La between 35.5 and 91.3 ppm and between 40.5 and 71.9 ppm, respectively) while they have similar MREE and HREE contents (Yb between 1.56 and 3.43 ppm and between 1.83 and 4.11 ppm, respectively). Volcaniclastics commonly show higher Rb (121–272.9 ppm) and Pb (4.5–137.1 ppm) with respect to lavas (Rb = 96.1–232 ppm and Pb = 2.7–45.8 ppm). Volcaniclastics are enriched in LILE, Th and U with respect to MORB (Fig. 13; normalization to MORB from Hofmann, 1988), with the exception of Sr, which commonly show a pronounced negative anomaly ($(Sr/Sr^*)_N$ = 0.55–0.05). The Sr negative anomaly is consistent with feldspar fractionation. Negative anomalies are also present for Nb and Ta, while Ba and Pb are commonly enriched (Fig. 13). Lavas show a similar trace pattern, but higher values dispersion (Fig. 13). The Ba enrichment is less pronounced with respect to volcaniclastics (Ba between 75 and 1965 ppm and 310–2245 ppm, respectively) and the Nb/Ta ratio show higher dispersion (3.29–14.63 and 6.73–13.9, respectively), indicating more limited fractionation of feldspar. Geochemical affinity of Tapajós volcaniclastics and lava flows suggests that the magmatism occurred in active continental setting (Fig. 14). Using the tectonic discriminant diagrams of Zr + Nb + Ce + Y (ppm) vs FeOtot/MgO (wt %), Yb vs Ta and Th-Ta-Hf/3 (Whalen et al., 1987; Pearce et al., 1984; Wood, 1980), the magmatism in the Tapajos region appears related to a syn- to post-collisional setting with few samples falling into the intraplate field (Fig. 14). According to the refined diagram Nb + Y vs Rb of Pearce (1996), all the Tapajos volcanics, together with the majority of volcanic rocks from the Sobreiro formation (Fernandes et al., 2011) are consistent with a late- to post-collisional setting (Fig. 14).

9. U-Pb zircon Geochronology

Zircons from Tapajos samples are colorless, sometimes fractured and euhedral to sub-euhedral. They can contain inclusions of apatite or

Table 1
Summary of the main characteristics of volcaniclastic lithofacies of the primary and secondary products analyzed and their interpretation.

		Lithofacies	Description	Interpretation
Primary volcaniclastic rocks	Massive	**mAL** Massive Ash to Lapilli	Massive fine and coarse ash and variable fine to coarse lithic lapilli content. Devitrified fragments immersed. Brocken crystal (plg/prx) content. Moderate to bed sorting.	The massive fine aspect suggests deposition from a dilute pyroclastic density current (PDC). Brocken crystals confirm the fragmental character. Granular flow regime.
		mLA Massive Lapilli and Ash	Massive, fine, fine to coarse and coarse devitrified lapilli immerse in ash matrix, less blocks immersed, maximum size 20–25 cm. Moderate sorting.	The massive aspect suggests deposition from a dilute PDC. The coarser character could be also related to proximal co-ignimbritic breccias as result of deposition by denser pyroclastic granular flows.
		mLB, Massive Lapilli and Block	Massive, monolithologic, angular coarse lapilli and blocks (50–60 cm) immersed in lapilli matrix. Moderate sorting.	Basal auto-brecciation of lava flows and/or rheo-ignimbrite flows
		Welded ignimbrites *l-g***wLA**, *m-g***wLA**, *h-g***wLA** low-, medium-, high-grade welded Lapilli and Ash	Massive, fine to coarse, moderately to strongly flattened devitrified lapilli (*fiamme*) varying from millimetric to 3–4 cm in size and lithic lapilli and ash. Crystal content. Clasts are immersed in a homogeneous ashy matrix. Low- to high-grade welded deposits. Eutaxitic texture. Moderate sorting.	The massive aspect suggests deposition from a pyroclastic density current. Welding is the result of post-depositional loading and are favored by low-viscosity pyroclasts that are promoted by high emplacement temperature, porosity and dissolved water.
	Banded	rheo-**ign** Rheoignimbrite (lava-like)	Layering of thin, dark and light bands and boudinaged fiamme. Parataxitic fabric displays subhorizontal bands and intricate small-scale intrafolial folds are present. The bands are deformed and flattened around lithic fragments and crystals.	The vitric fragments immersed in the welded ignimbrite distort and stretch up to the volcaniclastic flow becomes banded and starts to flow viscously.
	Stratified	**sA** Stratified Ash	Stratification of millimetric fine, devitrified, angular, sharply ash fragments.	The stratification is due to the bedding of shards fragments from a fall-out activity or from a dilute ignimbrite cloud.
		dsAL Diffusely stratified Ash to Lapilli	Diffusely stratified lithic and devitrified coarse ash and lapilli. Thickness of individual bedding surfaces ranges between few to several centimeters. Moderate sorting.	The diffuse stratification could indicates a flow boundary which is influenced by traction processes such as for pyroclastic density currents. Fall-out deposit (?).
		xsA Cross-stratified Ash	Cross-stratified fine ash formed by angular and sharply devitrified fragments (shards). Cross stratification is discontinuous over decimeters in macro-scale and as well as over millimeters in microscopic scale. Well to moderate sorted.	The internal cross-stratification indicates a grain by grain deposition process from a turbulent current with a flow boundary zone dominated by traction mechanism. Pyroclastic density currents (surge).
Secondary volcaniclastic/epiclastic rocks	Massive	**mS** Massive Sand	Massive quartzitic sand, good sorting. No internal structures. Centimeter ripples at the top of the strata.	Continental supply in a shallow, low energy, water sedimentary setting. Subaerial to sub-aqueous transition.
		csG Clast supported Gravel	Clast supported polimictic gravel with rounded clasts, good sphericity and sorting. Clasts are mainly characterized by massive and banded felsic lava fragments.	Clast-supported with minor matrix content is indicative of water flow. Shallow water to subaerial. Laminar debris-flow regime in a medial reaches of stream-dominated fluvial/alluvial fans.
		csGS Clast supported Gravel to Sand	Clast supported polimictic, gravel to coarse sand with sub-rounded/sub-angular fragments, low-medium shericity.	Clast-supported with minor matrix content is indicative of water flow. Deposition within a debris-flow dominated fluvial/alluvial environment.
		csGC Clast supported Gravel and Cobble	Clast supported polimictic, gravel and cobble with sub-rounded fragments (<20 cm), low-medium shericity, low-sorted.	Water removed the finer particles during transport and deposition. Deposition within a debris-flow dominated alluvial environment.
	Stratified	**xsS** Cross-stratified Sand	Low angle cross-stratified quartzitic sand, good sorting. Layers ranges between millimeters to centimeters.	Wave-induce structure in a coastal sub-aqueous marine-basin environment or fluvial channels environment in low energy regime.
		xsSG Cross-stratified Sand and Gravel	Fine to coarse sand and fine crystal-lithic gravel, poor sorting, layers ranges between millimeters to centimeters.	Low to medium energy processes. Hyperconcentrated flood in stream reworking setting.
		dsSt Diffusely layered Silt	Diffusely millimetric layered silt. Presence of ripples and low energy wave structures, good sorting.	Shallow water basin, sedimentation in lacustrine basin and/or ponds. Some turbidite sedimentation.
		bChS Bedded Chert (and Sand)	Bedded chert with local sand contribution. Thinly multicolor laminated deposit with <1 mm microcrystalline quartz-dominate layers.	Precipitation of silica particles in closed lake basins in association with volcanic rocks and sandstone.

spinel and display commonly low emission in Cathodoluminescence (CL). All crystals show magmatic oscillatory zoning and commonly a dark core which, in most cases, appears to be homogenous. Nonetheless, in few cases an inner core with discordant and partially reabsorbed domains is recognized. Some of the zircons also show a bright CL rim with transgressive or sub-concordant contacts with the inner oscillatory zoning. Zircons from sample XU08 from the Xingu region are colorless, rarely fractured and sub-euhedral. Inclusions of apatite or spinel are also observed sometimes. Crystals are medium in CL emissions and commonly show a homogeneous core and a concordant magmatic oscillatory zoning. Few zircons show a core with discordant zoning. No transgressive bright CL rims were recognized. Analyses were carried out on zircons that do not show transgressive or resorption features and discordant inner cores. Zircons from sample NP183 (Ignimbrite) provide 4 discordant and 7 concordant analyses that provide an upper intercept at 1984 ± 8.5 Ma (95% confident decay-const. errs included, MSWD 1.09) and a concordia age at 1986 ± 8.2 Ma (2σ, decay-const. errs included, MSWD 1.08, Probability of concordance = 0.30;

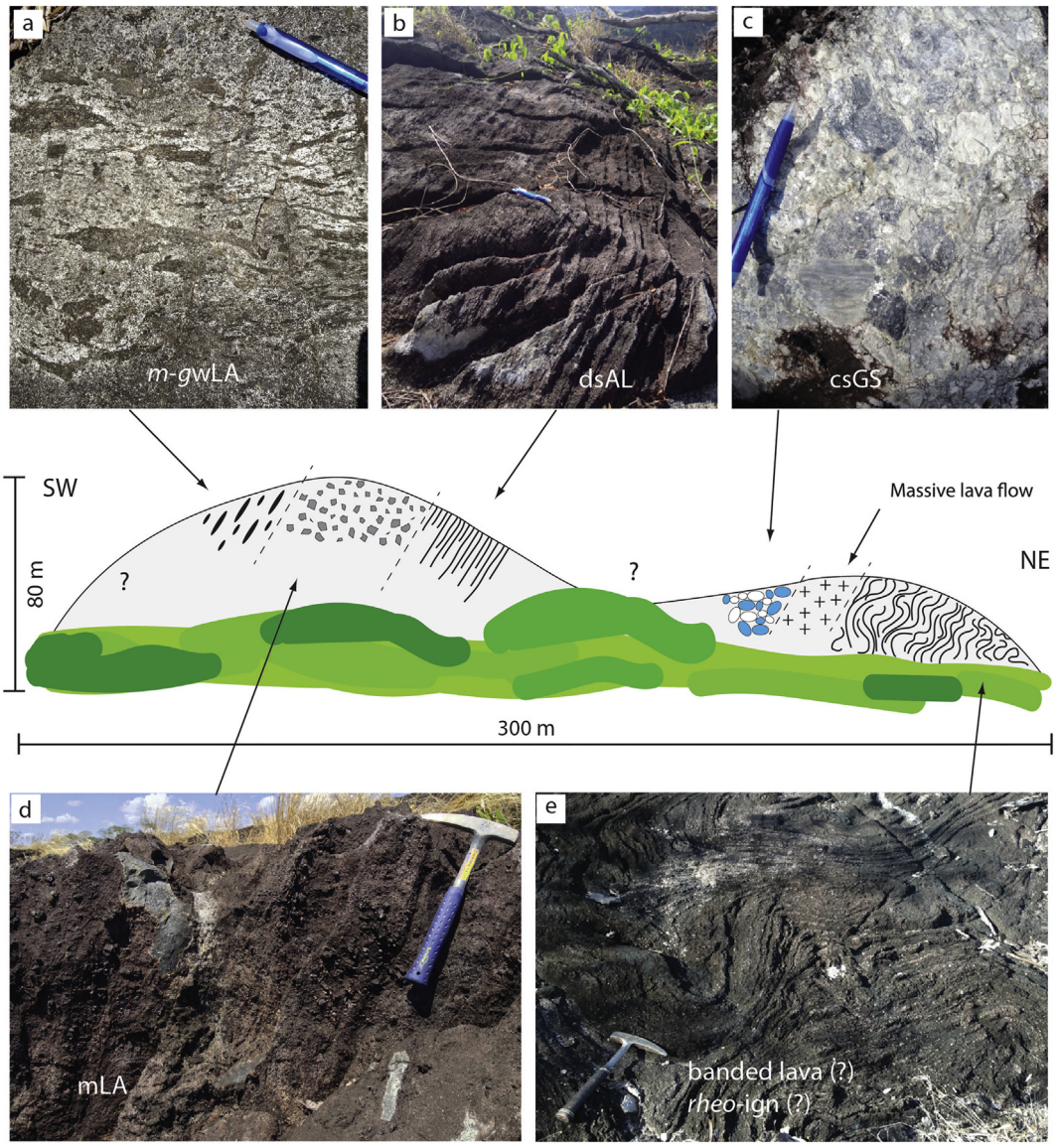

Fig. 11. Sketch of a wide (300 × 80 m) outcrop in the TMP (Np407; 6°40′35.21″ S, 55°21′14.63″ W). The stratigraphic sequence is tilted showing sub-vertical contacts of the different deposits. The sequence is interpreted displaying at the base banded (or rheo-ignimbrite) and massive lava flows passing to fragmental deposits to the top. a) ignimbrite medium-grade welded; b) the diffuse-stratified lithofacies indicates tractive processes usually attribute to pyroclastic surge-type depositional condition from dilute currents; c) sedimentary clast-supported deposit; d) non-welded lapilli to ash ignimbrite; e) banded lava o highly reomorphic ignimbrite (lava-like). For a more detailed lithofacies description see the text and Table 1.

Fig. 15). Single spot $^{206}Pb/^{207}Pb$ ages range between 2010 ± 17 Ma and 1909 ± 53 Ma with an average age of 1985 ± 11 Ma (95% confident decay-const. errs included, MSWD 1.6, Probability of concordance = 0.15; Fig. 15). Zircons from sample NP380 (Ignimbrite) show slightly older single spot $^{206}Pb/^{207}Pb$ ages between 2023 ± 31 Ma and 1981 ± 24 Ma with an average age of 1998 ± 5.9 Ma (95% confident decay-const. errs included, MSWD 0.74, Probability of concordance = 0.68; Fig. 15). Analyses are slightly discordant (up to 4%) providing an upper intercept at 1998 ± 7.7 Ma (95% confident decay-const. errs included, MSWD 0.74). Zircons from sample NP396 (Banded lava) provide 5 discordant ages and 8 concordant analyses, which provide an upper intercept at 1994 ± 8.2 Ma (95% confident decay-const. errs included, MSWD 1.40) and a concordia age at 1997 ± 7.0 Ma (2σ, decay-const. errs included, MSWD 5.70, Probability of concordance = 0.02; Fig. 15). Single spot $^{206}Pb/^{207}Pb$ ages range between 2014 ± 14 Ma and 1973 ± 8 Ma with an average age of 1994 ± 8.7 Ma (95% confident decay-const. errs included, MSWD 1.6, Probability of concordance = 0.12; Fig. 15). Pooling together the analyses of the Tapajós samples provides an average age of 1991 ± 12 Ma (2σ, MSWD 1.50, Probability of concordance = 0.06). Zircons from sample XU08 (Lava flow) provide a concordia age at 1882 ± 6.4 Ma (2σ, decay-const. errs included, MSWD 2.70, Probability of concordance = 0.10; Fig. 16). Single spot $^{206}Pb/^{207}Pb$ ages range between 1899 ± 10 Ma and 1875 ± 13 Ma, with an average at 1884 ± 5.2 Ma (95% confident decay-const. errs included, MSWD 0.60, Probability of concordance = 0.82).

10. Discussion

10.1. Subduction-related to extensional setting

The geochemistry of the TMP samples presented in this work display a high-K calc-alkaline signature (Fig. 12); they mainly fall into the A-type intra-plate granite field and tectonic discriminant diagrams suggest a late- to post-collisional setting for the TMP volcanism (Fig. 14). This interpretation is also supported by enrichment in LILE, Th, U and LREE of our samples, which suggest a strong crustal component in the

Table 2
Major and trace element bulk rock composition of Tapajos samples. Class identify the lithological features of the rocks: VC: volcanoclastic; I: ignimbrite; R: rhyolite; Type identify the geochemical affinity according to the granite classification (Zr + Nb + Ce + Y (ppm) vs FeO_{tot}/MgO (wt%) diagram, Fig. 14): I is for I-type granites and A is for A-type granites; b.d.l. is below detection limits; Mg# is calculated as Mg^{2+} / (Fe^{2+}_t + Mg^{2+}); (*) major elements analyses already published in Roverato et al. (2016).

Region	Tapajos										
Sample	NP – 079*	NP269a	Np380b	Np411c	NP-CO67*	NP - 080C	NP – 084A*	NP – 101*	NP - 123	NP - 156B*	NP - 159B
Class	VC	I	I	I	I	I	I	I	I	I	I
Type	A	A	A	A	A	A	A	A	A	A	A
XRF (%)											
SiO_2	71.80	68.78	72.20	66.36	70.81	70.80	68.15	72.22	72.80	71.59	65.48
TiO_2	0.34	0.32	0.35	0.72	0.40	0.40	0.48	0.32	0.31	0.36	0.58
Al_2O_3	14.16	15.37	14.24	15.57	14.76	14.52	15.43	14.28	13.59	14.27	18.22
Cr_2O_3	b.d.l.	b.d.l.	b.d.l.	b.d.l.	b.d.l.	b.d.l.	b.d.l.	b.d.l.	b.d.l.	b.d.l.	b.d.l.
FeOt	1.41	1.81	1.48	3.64	1.53	1.59	2.02	1.34	1.64	1.39	2.86
MnO	0.04	0.02	0.05	0.07	0.09	0.07	0.09	0.04	0.06	0.04	0.04
MgO	0.32	0.25	0.29	0.90	0.35	0.31	0.54	0.25	0.37	0.19	1.10
CaO	1.04	0.15	0.94	1.49	0.91	0.63	0.98	0.59	1.29	0.50	0.14
Na_2O	3.75	2.80	4.31	4.57	4.42	4.07	4.56	4.12	2.28	3.63	2.14
K_2O	5.73	6.00	5.32	3.73	5.71	5.77	5.63	5.60	5.04	5.60	6.06
P_2O_5	0.04	0.06	0.05	0.22	0.07	0.06	0.09	0.04	0.06	0.04	0.10
LOI	0.99	3.51	0.32	1.30	1.03	1.48	1.34	0.82	2.59	1.28	3.42
Tot	99.62	99.07	99.55	98.57	100.08	99.70	99.31	99.62	100.03	98.89	100.14
Mg#	0.29	0.20	0.26	0.31	0.29	0.26	0.32	0.25	0.29	0.20	0.41
ppm											
V	20	11	11	34	14	17	29	13	28	10	38
Co	34	38	2	15	17	31	29	43	25	32	12
Ni	1.20	2.50	0.50	0.50	0.40	0.70	0.90	0.80	0.60	0.60	2.80
Zn	28	33	45	71	55	50	55	36	33	27	55
Rb	185	194	179	121	155	144	122	191	230	174	273
Sr	221	188	209	557	141	124	187	174	172	148	127
Y	15	15	22	23	21	22	21	22	37	15	35
Zr	267	241	277	245	361	371	440	276	224	272	401
Nb	13	15	14	12	12	13	11	14	13	14	18
Cs	2.10	1.20	2.30	3.0	2.70	2.10	2.80	2.60	15	2.10	7.1
Ba	673	945	1425	1536	2185	1813	2245	1365	898	1362	1202
La	53	67	56	57	64	72	79	51	70	38	72
Ce	100	98	111	110	117	136	149	99	126	50	129
Pr	10	12	11	11	13	16	18	11	13	8.4	16
Nd	34	40	39	42	47	53	63	37	45	28	54
Sm	4.9	5.8	6.4	6.9	7.3	7.9	9.0	6.0	8.0	4.3	8.2
Eu	0.58	0.80	0.98	1.52	1.83	1.58	2.36	0.90	1.23	0.64	1.67
Gd	3.6	4.1	5.0	5.4	5.4	5.4	6.1	4.8	7.2	3.0	6.7
Tb	0.52	0.56	0.73	0.76	0.73	0.78	0.76	0.69	0.99	0.50	0.97
Dy	2.69	3.0	3.9	4.1	3.8	4.0	3.9	3.6	5.4	2.92	5.6
Ho	0.57	0.57	0.74	0.76	0.78	0.75	0.77	0.73	1.21	0.57	1.06
Er	1.61	1.65	2.19	2.17	2.08	2.33	2.19	2.21	3.3	1.77	3.3
Tm	0.24	0.26	0.35	0.36	0.33	0.34	0.34	0.36	0.48	0.29	0.48
Yb	1.56	1.83	2.38	2.22	2.30	2.12	2.08	2.41	3.43	1.95	2.90
Lu	0.24	0.29	0.38	0.35	0.36	0.36	0.34	0.36	0.54	0.33	0.49
Hf	7.7	7.0	7.3	6.4	8.4	8.5	8.9	7.2	6.3	7.6	9.8
Ta	1.50	2.20	1.00	1.50	1.00	1.40	1.20	1.70	1.50	1.80	1.30
Pb	23	6.3	13	7.3	24	73	20	10	26	9.2	4.5
Th	21	21	19	13	15	17	14	20	22	20	21
U	4.9	3.4	5.0	2.90	3.3	3.6	2.90	4.0	2.90	4.6	4.8

Region	Tapajos										
Sample	NP - 175A	NP – 176*	NP - 178B*	NP – 179*	NP – 180*	NP – 183A*	NP – 184*	NP - 093	NP - 094	Np272a	Np393A
Class	I	I	I	I	I	I	I	VC	VC	R	R
Type	A	I	A	A	A	A	A	A	A	A	A
XRF (%)											
SiO_2	73.86	75.93	70.86	72.53	69.73	71.25	70.99	60.36	62.46	71.13	76.57
TiO_2	0.24	0.20	0.39	0.37	0.44	0.41	0.37	0.81	0.89	0.49	0.09
Al_2O_3	13.40	12.71	14.62	14.44	15.20	14.65	14.54	15.42	16.36	14.44	11.93
Cr_2O_3	b.d.l.	b.d.l.	b.d.l.	b.d.l.	0.01	b.d.l.	b.d.l.	0.01	b.d.l.	b.d.l.	b.d.l.
FeOt	1.10	0.78	1.57	1.67	2.03	1.57	1.75	5.70	4.97	2.52	1.16
MnO	0.07	0.06	0.07	0.09	0.09	0.09	0.08	0.11	0.09	0.06	0.03
MgO	0.11	0.16	0.29	0.30	0.36	0.24	0.30	3.24	1.68	0.51	0.01
CaO	0.50	0.34	0.88	0.65	0.88	0.56	0.68	4.59	3.03	1.57	0.14
Na_2O	3.78	3.46	4.70	4.38	4.49	4.54	4.97	2.79	3.11	4.27	4.39
K_2O	5.41	5.11	5.11	5.56	5.64	5.57	4.87	4.67	5.86	2.32	3.95
P_2O_5	0.02	0.01	0.06	0.06	0.07	0.05	0.06	0.35	0.39	0.06	b.d.l.
LOI	1.15	0.88	1.28	0.85	1.00	0.81	1.07	1.37	0.64	1.38	0.58
Tot	99.64	99.64	99.83	100.90	99.94	99.74	99.68	99.43	99.48	98.75	98.85
Mg#	0.15	0.27	0.25	0.24	0.24	0.21	0.23	0.50	0.38	0.27	0.02

Table 2 (*continued*)

Region	Tapajos										
Sample	NP - 175A	NP – 176*	NP - 178B*	NP – 179*	NP – 180*	NP – 183A*	NP – 184*	NP - 093	NP - 094	Np272a	Np393A
Class	I	I	I	I	I	I	I	VC	VC	R	R
Type	A	I	A	A	A	A	A	A	A	A	A
ppm											
V	b.d.l.	b.d.l.	14	b.d.l.	17	b.d.l.	10	112	59	11	b.d.l.
Co	36	34	32	40	28	37	38	27	24	2.60	63
Ni	0.50	0.50	0.80	2.30	3.4	1.50	0.60	19	0.50	0.60	1.10
Zn	20	32	45	51	46	52	60	55	73	55	33
Rb	156	158	136	153	136	133	127	116	169	105	196
Sr	54	46	179	120	115	78	103	614	620	321	33
Y	27	20	23	27	22	23	20	16	23	21	37
Zr	223	162	397	370	423	402	360	174	257	279	181
Nb	13	13	13	14	11	12	12	7.3	11	12	23
Cs	3.2	3.9	2.10	3.10	2.60	1.80	0.70	4.2	6.2	1.70	1.60
Ba	477	310	2021	998	880	746	2243	1362	2063	1363	75
La	45	36	75	76	91	80	64	35	53	59	72
Ce	92	70	140	138	174	151	122	70	106	108	133
Pr	11	8.3	15	15	20	18	14	8.5	13	11	14
Nd	39	29	57	52	69	64	52	31	48	38	45
Sm	6.7	4.7	8.9	8.1	10	9.4	7.9	5.2	7.6	6.5	8.1
Eu	0.72	0.49	1.98	1.36	1.63	1.51	1.84	1.35	1.71	1.27	0.09
Gd	5.3	3.7	6.9	6.9	6.6	6.6	5.7	4.3	5.5	4.9	7.0
Tb	0.81	0.59	0.76	0.87	0.92	0.91	0.78	0.57	0.81	0.70	1.14
Dy	4.7	3.7	4.5	4.3	4.4	4.6	4.0	3.0	4.3	3.7	6.8
Ho	0.90	0.72	0.86	0.91	0.80	0.83	0.82	0.56	0.82	0.69	1.31
Er	2.63	2.25	2.73	2.57	2.23	2.31	2.51	1.52	2.32	1.99	3.9
Tm	0.41	0.35	0.39	0.36	0.36	0.37	0.36	0.23	0.32	0.31	0.62
Yb	2.61	2.21	2.44	2.71	2.25	2.43	2.32	1.43	2.08	1.95	4.1
Lu	0.39	0.33	0.42	0.43	0.36	0.40	0.37	0.24	0.33	0.30	0.60
Hf	6.6	5.2	8.7	8.5	9.6	9.3	8.4	4.3	6.2	7.1	7.4
Ta	1.80	1.70	1.10	1.80	1.40	1.60	1.60	0.60	1.00	0.90	7.1
Pb	16	29	137	10	17	11	28	4.0	6.9	46	36
Th	17	18	17	16	16	17	17	6.1	11	13	30
U	3.4	4.4	3.5	3.9	3.5	3.7	4.0	1.30	2.10	3.4	9.1

Region	Tapajos								
Sample	Np405	Np406	NP - 039B	NP - 073	NP - 114	NP - 121	NP – 173*	NP - 175B	NP - 182C
Class	R	R	R	R	R	R	R	R	R
Type	A	A	A	A	A	A	I	I	I
XRF (%)									
SiO_2	73.67	69.79	65.32	72.82	63.80	75.09	75.58	75.03	74.44
TiO_2	0.33	0.45	0.86	0.31	0.74	0.27	0.20	0.22	0.22
Al_2O_3	13.09	14.72	16.61	13.84	17.99	13.16	12.96	13.46	13.50
Cr_2O_3	b.d.l.	b.d.l.	b.d.l.	b.d.l.	b.d.l.	b.d.l.	b.d.l.	b.d.l.	b.d.l.
FeOt	1.33	1.78	3.27	1.29	3.30	1.01	0.99	0.96	1.23
MnO	0.05	0.05	0.09	0.04	0.05	0.03	0.07	0.09	0.02
MgO	0.26	0.30	0.51	0.28	0.70	0.10	0.19	0.19	0.14
CaO	0.53	0.76	2.07	0.89	1.54	0.15	0.72	0.42	0.04
Na_2O	2.25	3.87	4.99	3.61	5.02	3.78	3.21	3.69	3.56
K_2O	7.13	5.57	3.88	5.71	5.51	5.19	5.18	5.39	4.92
P_2O_5	0.03	0.07	0.22	0.04	0.22	0.03	0.02	0.02	0.02
LOI	0.55	1.26	1.50	0.75	1.45	0.95	1.49	0.83	2.09
Tot	99.22	98.62	99.32	99.58	100.32	99.76	100.61	100.30	100.18
Mg#	0.26	0.23	0.22	0.28	0.27	0.15	0.25	0.26	0.17
ppm									
V	8	<8	55	14	83	18	<8	<8	<8
Co	1.00	36	19	19	14	52	25	45	100
Ni	0.40	2.40	2.20	3.60	1.90	0.60	0.70	0.70	1.30
Zn	30	38	49	21	48	18	16	28	8
Rb	232	194	96	200	153	190	156	158	133
Sr	204	229	552	193	377	91	79	63	32
Y	23	22	20	18	26	34	64	24	18
Zr	272	336	228	246	265	245	173	191	189
Nb	14	15	9.2	14	12	17	13	14	13
Cs	2.20	2.50	2.10	2.30	1.30	3.1	4.1	3.5	1.10
Ba	1634	1965	1615	534	1918	583	485	413	569
La	63	62	50	57	58	62	48	41	41
Ce	120	117	96	101	107	112	76	80	80
Pr	12	12	11	11	13	13	10	10	10
Nd	43	42	38	38	49	45	34	32	32

(*continued on next page*)

Table 2 (*continued*)

Region	Tapajos								
Sample	Np405	Np406	NP - 039B	NP - 073	NP - 114	NP - 121	NP – 173*	NP - 175B	NP - 182C
Class	R	R	R	R	R	R	R	R	R
Type	A	A	A	A	A	A	I	I	I
Sm	6.6	6.9	6.4	5.6	7.5	8.4	5.4	5.8	5.4
Eu	0.93	1.27	1.68	0.68	1.70	0.87	0.69	0.53	0.66
Gd	5.2	5.3	5.1	4.5	5.8	7.0	5.0	4.6	3.8
Tb	0.73	0.74	0.69	0.55	0.80	1.02	0.80	0.76	0.58
Dy	3.9	4.0	3.8	3.0	4.4	6.1	5.2	4.2	3.6
Ho	0.82	0.79	0.79	0.58	0.94	1.25	1.17	0.80	0.66
Er	2.21	2.31	2.31	1.76	2.64	3.4	3.8	2.42	2.02
Tm	0.35	0.34	0.34	0.27	0.39	0.52	0.56	0.36	0.31
Yb	2.47	2.28	2.01	1.83	2.43	3.3	3.1	2.43	2.03
Lu	0.39	0.37	0.30	0.26	0.35	0.53	0.54	0.36	0.33
Hf	8	9.3	5.9	7.3	6.3	7.6	5.5	6.0	5.3
Ta	1.00	4.5	1.00	1.50	0.80	2.30	1.60	2.20	1.50
Pb	10	11	10	19	8.6	16	13	9.2	2.70
Th	20	17	12	24	14	23	19	17	17
U	4.5	3.9	2.90	5.4	3.2	6.9	5.0	4.2	2.70

parent melt consistent with a subduction/post orogenetic geodynamic setting (Figs. 12, 13, 14), and the high HSFE which shifted the TMP volcanics composition in the A-type granites showing however FeO/MgO which are low and comparable with I- and S-types granites (Fig. 14). Similar features are reported in previous works (Lamarão et al., 1999; Lamarão et al., 2002) for volcanics in the Tapajós region, which are grouped into the Vila Riozinho (VR) and Maraes Aldeida (MA) formations, respectively. The VR rocks are intermediate to felsic in composition (Lamarão et al., 2002) with a calc-alkaline signature, while the rhyolites and ignimbrites of MA are slightly enriched in silica compared to the rhyolites of VR and are geochemically similar to evolved A-type granites (Lamarão et al., 2002). Our results show similarities with these data, suggesting that our specimens could be part of the VR and/or MA formations. The identification of two volcanic series has important implications for the understanding of the magmatic evolution of the Amazonian craton in late Paleoproterozoic. A model for the evolution of the TMP involves a first stage of subduction-related magmatism followed by an intracontinental magmatism related to a distensional event (Lamarão et al., 2002). Geochronological analyses by Lamarão et al. (2002) yielded ages of ca. 2 Ga for the VR and ca. 1.88–1.87 Ga for the MA volcanisms. The three new U-Pb geocronological analyses reported in this study yielded ages of ca. 2000 Ma (Fig. 15) are concordant with the ages presented by Lamarão et al. (2002) for the VR magmatism, thus suggesting that the TMP rocks could be part of the VR volcanic sequence. However, TMP rocks are geochemically more evolved with respect to VR in terms of SiO_2 (63.8–76.6 wt% and 54.4–71.8 wt%, respectively), K_2O (2.3–7.1 wt% and 2.1–5.8 wt%, respectively) and REE abundances and are more similar to MA rocks (Figs. 11, 12 and 13). In particular, REE patterns of the TMP samples are comparable with the rocks of the MA formation (Fig. 12) while they are more enriched in REE with respect to VR rocks. Conversely, TMP rocks are enriched in Ba (Fig. 12), while MA are depleted, and have compositions for Rb/Zr ratio and Nb, considered as a proxy for arc maturity (Brown et al., 1984), similar to VR and different from MA (Rb/Zr between 0.3 and 1.1 in TMP, 0.2–0.7 in VR and 0.2–1.7 in MA; Lamarão et al., 2002). Thus, according to geochronological and petrological data, we proposed that the TMP rocks in this study must be ascribed to the VR formation. Geochemical differences in our rocks and VR volcanics could be explained by a more evolved character of the TMP rocks. The evidences of plagioclase fractionation from the parent melts of the TMP (negative Eu and Sr anomalies, Fig. 12) and their absence in less evolved VR rocks reinforce this interpretation, and suggest fractional crystallization as the prominent process controlling the VR magmatism evolution. However, we want to point out that due to the large area covered by the presented investigation (Fig. 2), together with the VR area, the geochemical variations between our rocks (TMP) and VR could be the result of local/regional heterogeneities in the magmatism. This hypothesis is supported by the intermediate characteristics of the TMP samples with respect to the VR and MA volcanoclastic material (Figs. 11, 12 and 13).

Recently, new authors (Juliani et al., 2014) suggest the geochemical and geocronological signature of the MA formation could be correlated to the felsic Santa Rosa formation (SRF) cropping out in the SFX region. Our new U-Pb geocronological analyses on one rock sample from the SRF yielded an average age of 1884 ± 5.2 Ma (Fig. 16) that is consistent with previous Pb-Pb ages on other locations. Juliani and Fernandes (2010) published two Pb-Pb ages on zircons of 1879 ± 2 Ma and 1884 ± 1.7 for a rhyolite and an ash tuff, respectively. Recently Antonio et al. (2017) publishes the first U-Pb ages on zircons for the Santa Rosa Formation with 1877.4 ± 4.3 Ma for a rhyolite and 1895 ± 11 Ma for a dike. All geochronological results support a ca. 1880 Ma age for the emplacement of these rocks.

The southern Amazonian craton, as well as other Precambrian terrains worldwide (Condie, 2002; Hofmann, 1988; Zhao et al., 2002), are considered to be characterized by a series of orogenic to post-orogenic events from 2.0 up to 1.88 Ga. The amalgamation of cratonic blocks worldwide established connections between South America and West Africa and other cratonic terrains such as Western Australia and South Africa, Laurentia and Baltica, Siberia and Laurentia, Laurentia and Central Australia, etc. (Zhao et al., 2002). These late-Paleoproterozoic collisional processes likely formed the controversial supercontinent Columbia (Zhao et al., 2004). This period also coincides with a major peak in orogenic gold resources (Goldfarb et al., 2001; Juliani et al., 2014) and understanding the geodynamic of this period is crucial for economic interests. Antonio et al. (2017) highlight that for the period 1.88 Ga, many cratonic terrains have been characterized by extensive magmatism. These authors report as examples the 1880 Ma NE-trending Ghost dike swarm and the 1880 Ma Circum-Superior LIP in the Canadian shield (Minifie et al., 2013), the 1880 Ma Southern Bastar-Cuddapah LIP in India (French et al., 2008), the Mashonaland sills and the Post-Waterberg dolerites in Kalahari craton (Hanson et al., 2004), an extensive A-type magmatism in Baltica and in Siberia. The A-type affinity of the 1.88 Ga rocks is widely described by other authors in different regions into the Amazonian craton (Ferron et al., 2010; Pierosan et al., 2011; Fernandes et al., 2011; Klein et al., 2012; Barreto et al., 2014; Teixeira et al., 2018). Currently, the significance of the 1.88 Ga A-type magmatism in the AC is still matter of debate, also due to the extremely large aerial cover which interested several different domains with different basements and geologic evolutions. For example, studies on the Carajas region suggest that the 1.88 Ga anorogenic

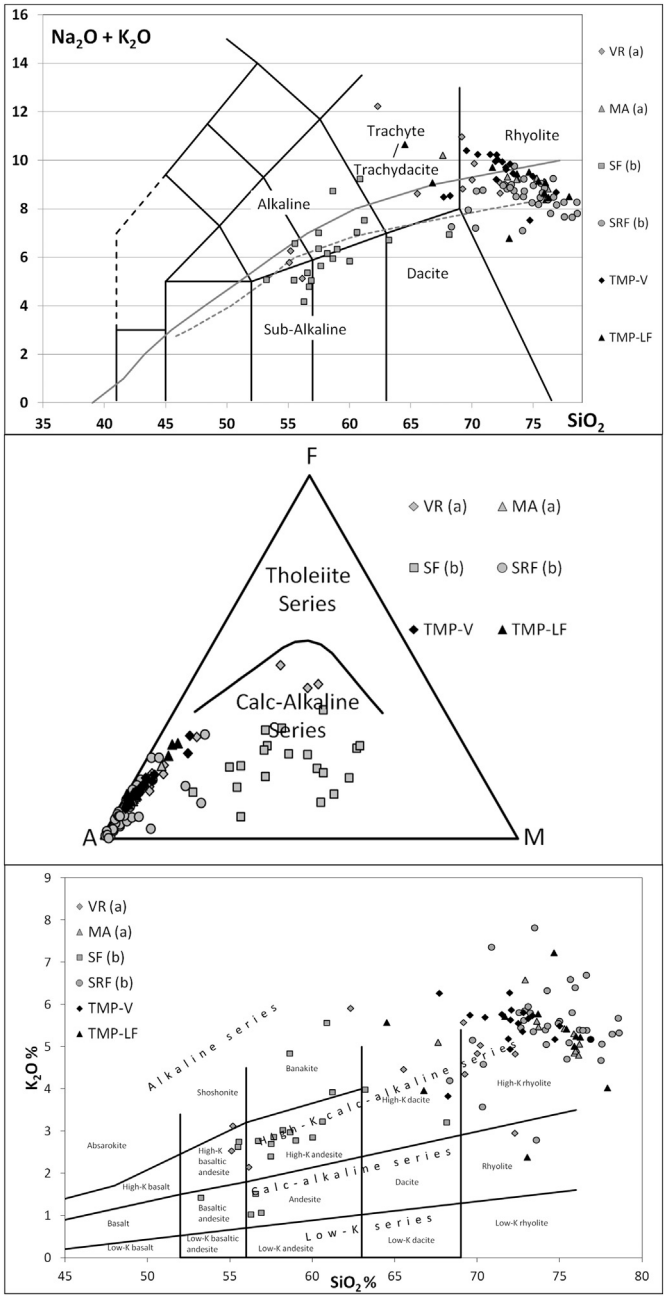

Fig. 12. Classification diagrams for the Tapajos volcanics (TMP-V) and lava flow (TMP-LF). TAS diagram with limits of alkaline series from Kuno (1968), dashed line, and Irvine and Baragar (1971), solid line. AFM diagram with alkaline field from Irvine and Baragar (1971). SiO_2 vs K_2O classification diagram (Ewart, 1982). Literature values are from: VR (a) Vila Rozinho and MA (a) Moraes Almeida volcanic sequences from Lamarão et al. (2002); SF (b) Sobreiro Formation and SRF (b) Santa Rosa Formation from Fernandes et al. (2011).

magmatism in this domain was provoked by delamination and fusion of the Archean basement by a mantle plume which originated an extensional setting (Dall'Agnol et al., 2005; Silva et al., 2016; Teixeira et al., 2018; Teixeira et al., 2019).

Conversely, the geochemical features of the TMP and SFX magmatism presented in this work and in literature (Lamarão et al., 2002, 2005; Fernandes et al., 2011) mainly support an extensional regime of these regions related to a late- to post-collisional event, being possibly related to the end of the subduction process. The transition from convergent (late-/post-orogenic) to extensional tectonic setting could register the beginning of the taphrogenesis that marked the Amazonian Craton throughout the Mesoproterozoic (Brito-Neves, 2011; Lamarão et al., 2002). The ca. 1.88 Ga felsic magmatism in different provinces of the Amazonian craton could represent the oldest magmatism related to this event.

It should be mentioned that in term of textural features, the products emitted during the transition between the late-/post-collisional to extensive events don't display substantial variations. In other words, the lithofaciological signature of the volcanic and volcaniclastic rocks that characterized the 2 Ga VR event (subduction related) is similar for those products erupted during the 1.88–1.87 Ga extensional volcanism that characterized the MA and SRF events. Moreover, the post-orogenic to extensional setting emphasizes the continental setting where the studied volcanic products have been emitted. Following the idea of Roverato et al. (2017) for the Late-Paleoproterozoic andesitic Sobreiro Formation, we stress the lack of any evidences in favour of subaqueous eruptions for the emitted felsic products such as pillow lavas as well as hyaloclastites. This suggests the subaerial character of the volcanism and its emitted products acted in both regions.

10.2. Eruptive style and emplacement

The study areas are widely characterized by volcanic deposits whose eruptive style is hard to differentiate. Distinguishing between banded lavas and high grade ignimbrites is, sometime, extremely challenging (Henry and Wolff, 1992; Manley, 1996). This is made even more complicated when the investigated deposits are ancient and the outcrops intensely eroded, such as those Precambrian terrains investigated here (Lenhardt et al., 2012; Roverato et al., 2016; Lenhardt et al., 2017). Evidences in the field show that a great volume of the volcanic activity is represented by the emission of lava flows and/or high-grade to rheomorphic ignimbrites, although an important amount of other fragmental products of different type (Lf mAL, mLA, *l-g/m-g/h-g*wAL) are also well represented in both regions. High-grade welded and rheomorphic (up to lava-like) ignimbrites share similar features with lavas, displaying banding and ductile folds formed by the elongation of fiamme and vesicles (Schmincke and Swanson, 1997; Chapin and Lowell, 1979; Wolff and Wright, 1981; Branney and Kokelaar, 1992; Sumner and Branney, 2002; Pioli and Rosi, 2005; Andrews and Branney, 2011; Brown and Bell, 2013). Although the ignimbrites investigated here have a fragmental derivation their origin largely differ from those characteristic of fallout deposits that form by a sustained column explosive-driven eruption. High-grade welded and rheomorphic ignimbrites are correlated with highly explosive plinian-type eruptions which produce, during their column collapse stage, large PDC. In addition, high-grade rheomorphism of silicic products, either deriving from an explosive or effusive eruption, are favored by high temperature low-viscosity emplacement conditions and the presence of some residual water. The high temperatures condition of our deposits is also confirmed by the pervasive presence of spherulites and lithophysae formed during the slow-cooling regimes of large silica-rich lavas and welded ignimbrites (Lofgren, 1971; Breitkreuz, 2013). The eruptive scenario showed in Fig. 17 giving origin to the frequent eruption of large volume and high discharge rate lava flows and ignimbrites was likely characterized by fissure-fed and caldera collapses systems as those described by previous authors (Legros and Kelfoun, 2000; Aguirre-Diaz and Labarthe-Hernández, 2003; Cas et al., 2011; Lesti et al., 2011; Lenhardt et al., 2012; Willcock et al., 2013). Eruptions fed by extensive fissures of large size, in fact, appear to be the most favourable volcanic systems to minimize cooling during emplacement and produce an alternance of low-height sustained column eruptions feeding PDC and eruptions characterized by the effusion of low viscosity lava flows, coulees and domes, while maintaining high discharge rates (e.g. Bachmann et al., 2000; Aguirre-Diaz and Labarthe-Hernández, 2003; Polo et al., 2017a, 2017b; Simões et al., 2017). The sustained fountaining and entrainment of air in the eruptive jet is strongly influenced by the geometry of the conduit (Legros and Kelfoun, 2000) as well as the transition from sustained to collapsing eruptive column. A wide-geometry conduit

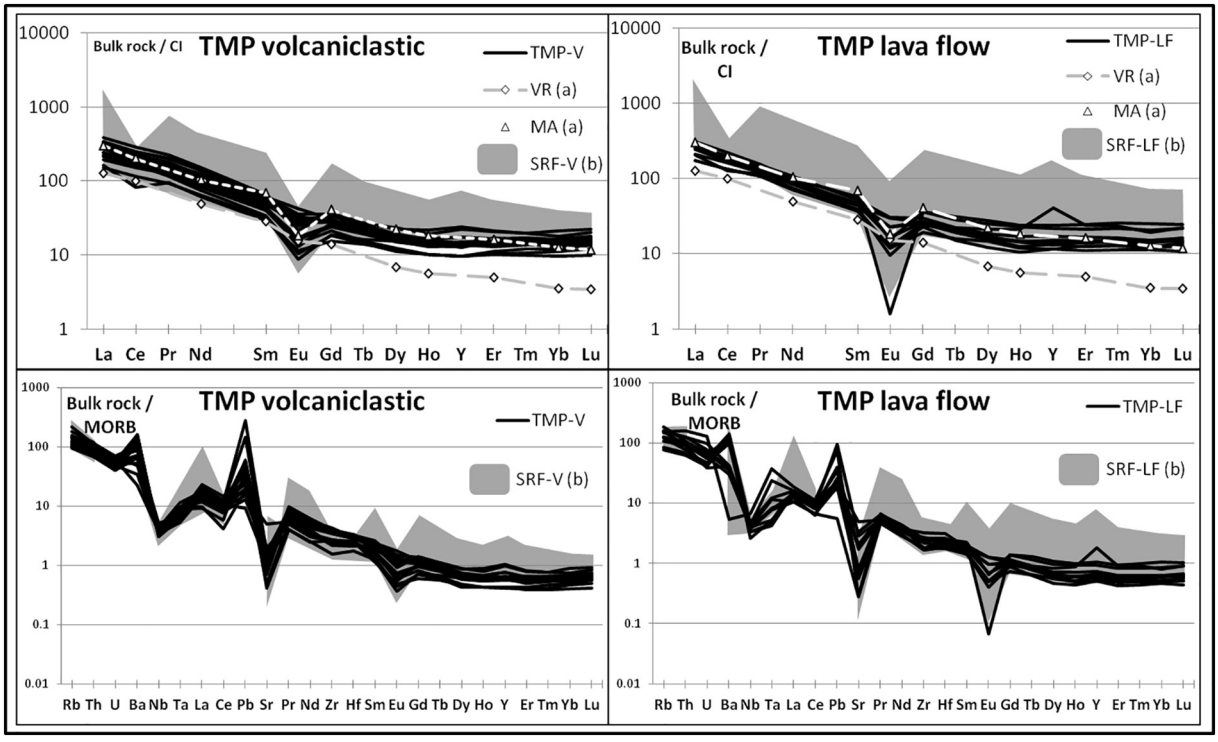

Fig. 13. REE and spider-diagrams of volcanics and lava flow rocks from the Tapajos region (TMP-V and TMP-LF). REE data are normalized to Chondrite I (CI; values from Anders and Ebihara, 1982) and trace elements are normalized to Mid Ocean Ridge Basalt (MORB; values from Hofmann, 1988). Literature values are from: VR (a) Vila Rozinho and MA (a) Moraes Almeida volcanic sequences are average values from Lamarão et al. (2002); SRF (b) Santa Rosa Formation from Fernandes et al. (2011) divided in -V volcanoclastics and -LF lava flow. Due to the lack of literature data, comparison of VR (a) and MA (a) is reported only for REE diagram.

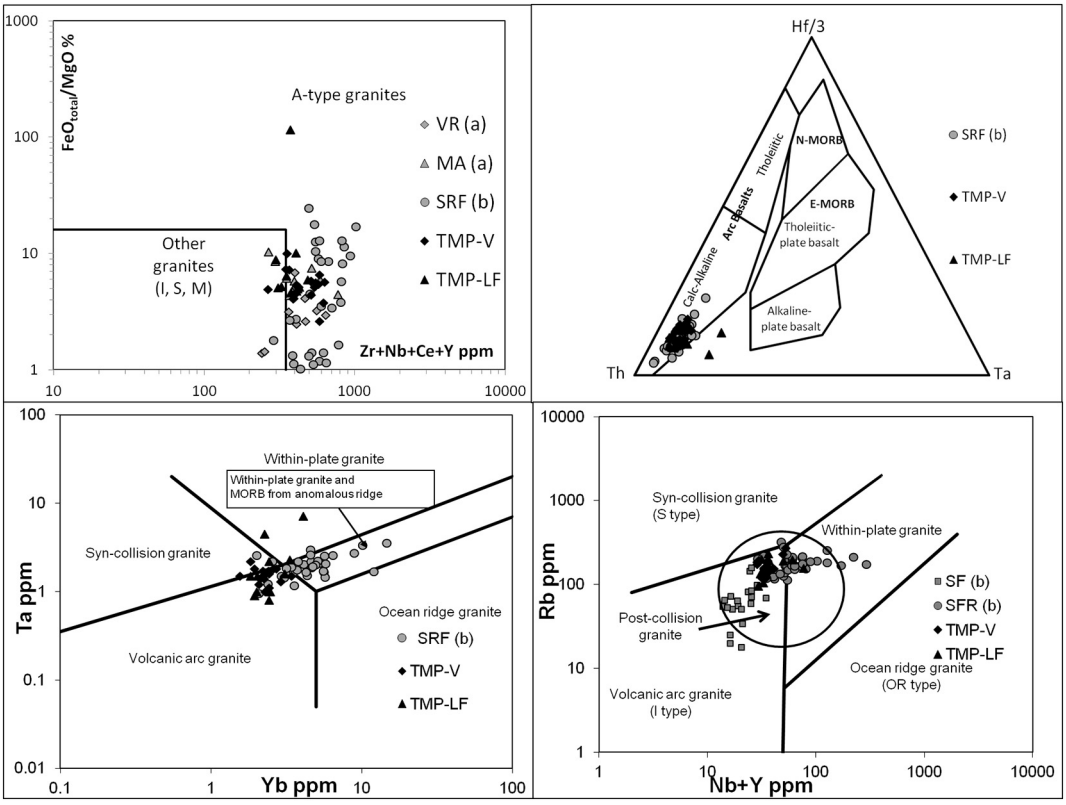

Fig. 14. Tectonic affinity discriminant diagrams for the Tapajos volcanics (TMP-V) and lava flow (TMP-LF). Zr + Nb + Ce + Y (ppm) vs FeO_{tot}/MgO (wt%) diagram. Yb vs Ta diagram. La/Yb vs Nb/La diagram. Th-Ta-Hf/3 diagram. Literature values are from: VR (a) Vila Rozinho and MA (a) Moraes Almeida volcanic sequences from Lamarão et al. (2002); SF (b) Sobreiro Formation and SRF (b) Santa Rosa Formation from Fernandes et al. (2011).

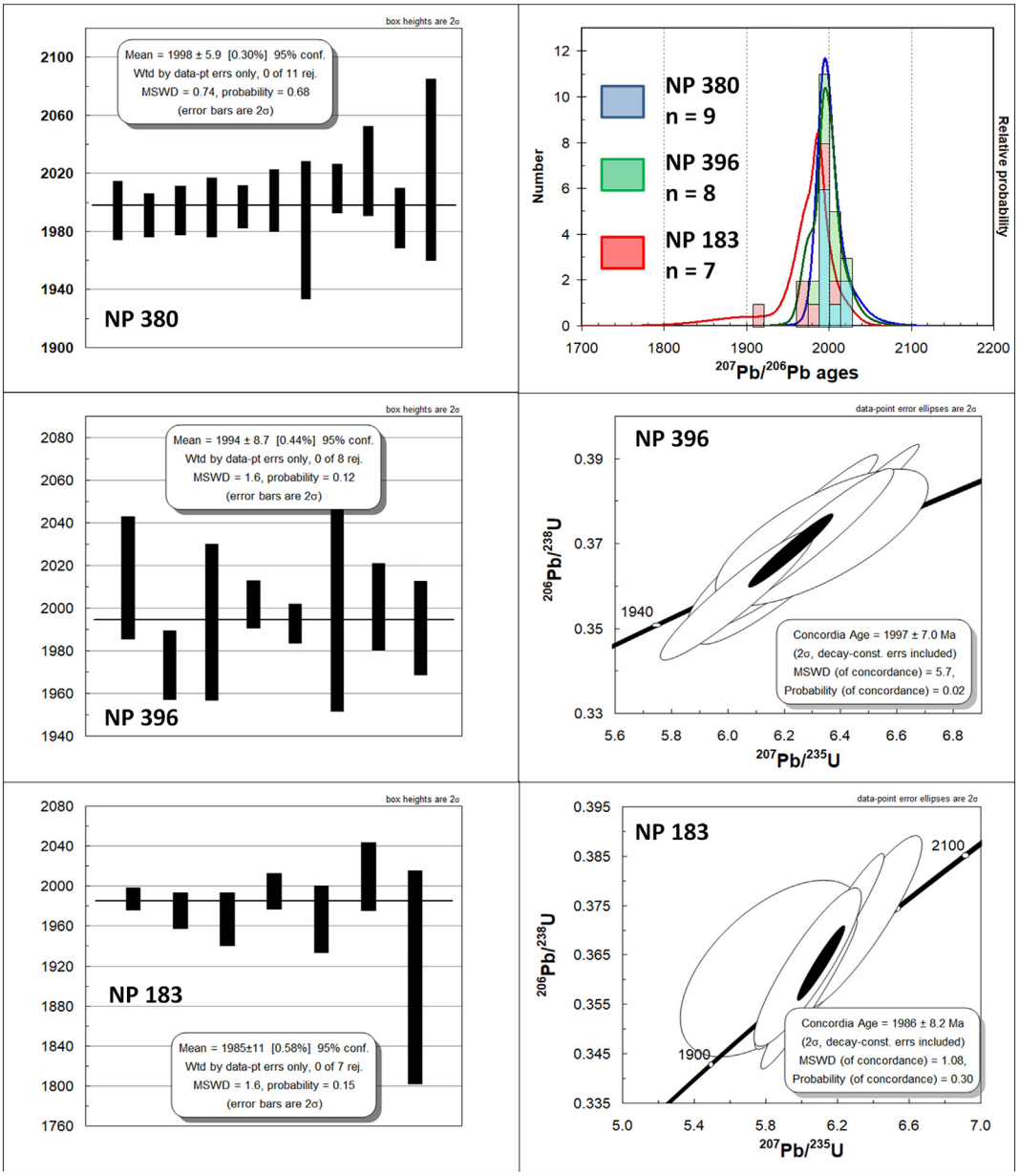

Fig. 15. Geochronological U-Pb data from Tapajos zircons. Average $^{206}Pb/^{207}Pb$ age (errors are calculated as 2σ) of the three samples. Probability density plot of $^{206}Pb/^{207}Pb$ ages. Calculated concordia age for sample NP396 (lava flow) and NP183 (ignimbrite).

would impede much air entrainment into the pyroclastic fountain and, at the same time, would favors magmatic escape of volcanic gases, favoring the low fountaining and promoting a "boil-over" style eruption (Branney and Kokelaar, 1992, 2002; Lenhardt et al., 2017) with high discharge rate. Moreover, the low air injection would inhibit the dilution of the eruptive material making it thermodynamically isolated from the surrounding environment (Lesti et al., 2011), preserving the high temperatures and enhancing the agglutination of fragments (welding) (Quane and Russell, 2005; Russell and Quane, 2005; Giordano et al., 2005). When the low-altitude pyroclastic fountaining or the emission of high temperature lavas would be maintained for long time the high flow-mobility is ensured (Sulpizio et al., 2014). If the material supply from the vent continues for long time and with high discharge rate, the mobility could be maintained even on very low slope angles (Sulpizio et al., 2014; Giordano et al., 2017; Kolzenburg et al., 2017), and flowing various kilometers up to hundreds of kilometers far from the vent (Aguirre-Diaz et al., 2008; Cas et al., 2011; Giordano et al., 2017). This could explain the presence of large silicic volcanic areas characteristic of the ancient Amazonian volcanism (Roverato et al., 2016). Although, volcaniclastic rocks seem to be volumetrically less important in the study areas than the lava flows and/or rheomorphic ignimbrites the recognition of fragmental rocks during our field campaigns is important to understand their significance into our paleogeographic reconstruction (Fig. 17). An idealized deposit sequence of a caldera forming eruption displays an air-fall deposit overlain by an ignimbrite (Druitt and Sparks, 1984) and the transition from the sustained column phase to the pyroclastic flow phase is often accompanied by a strong increase in the discharge rate (Bursik and Woods, 1996). The stratigraphic sequence of Fig. 11 shows this association of a possible air-fall deposit (Lf dsAL) linked with pyroclastic flow-dominated deposits (Lf mAL and *m*-gwLA). In some cases, pyroclastic eruptions commonly precede lava emplacement (Fink, 1983; Heiken and Wohletz, 1987). The sequence presented in Fig. 7 shows a low-grade welded ignimbrite deposit (Lf *l*-gwAL) overlaid by a thick banded body that we are interpreting here as a lava flow. At the base of the banded lava is a breccia (Lf mLB) consisting of clasts of a mix of lava

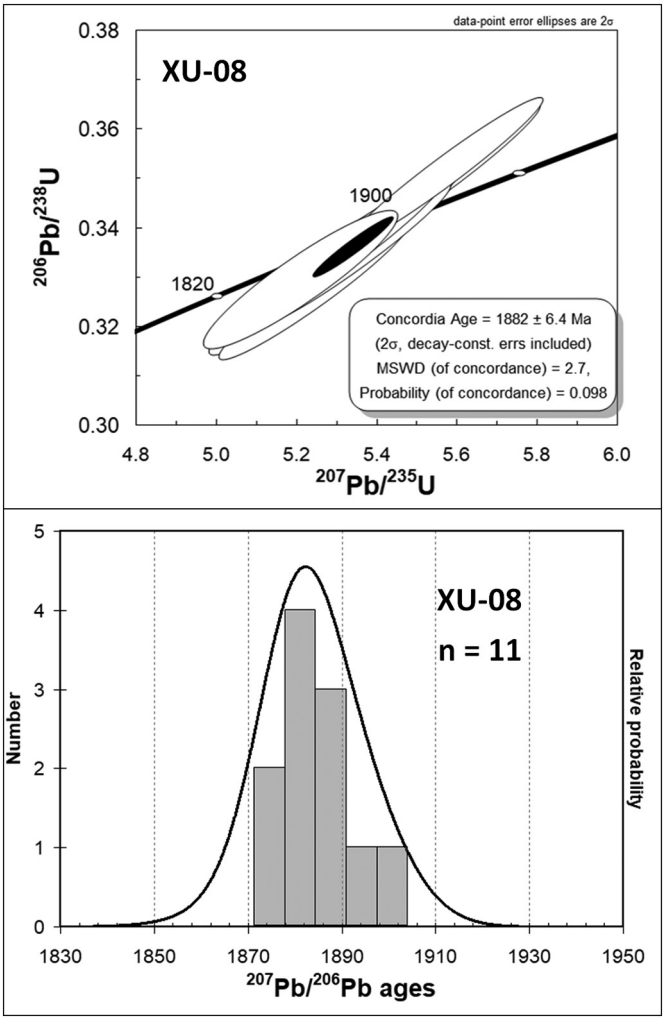

Fig. 16. Geochronological U-Pb data from Xingu zircons. Calculated concordia age for ignimbrite sample XU-08. Probability density plot of $^{206}Pb/^{207}Pb$ ages.

textural types, including massive, vesicular, flow banded and flow-folded, glassy, pumiceous and devitrified. Autobrecciation in lavas or rheomorphic ignimbrites occurs when more rigid layers and the external parts are broken in response to the applied shear stress locally exceeding the tensile strength (Fink and Manley, 1987). Some polymictic breccia deposits (Lf mLA) are characterized by lithic angular clasts and devitrified fragments that could point to co-ignimbritic breccias with short transport of the emitted material. These deposits could be also related to collapse-caldera-breccias falling down into the caldera ring during the roof subsidence. Air-fall (sA) and dilute pyroclastic flow (xsA) deposits (surge type) crop out in both regions. These, linked with the glassy and lithic pyroclastic material described above, are evidence of intense explosive phases from more sustained column eruptions of smaller intra-caldera volcanic centers and/or associated to events of caldera collapse (Fig. 17).

10.2.1. The sedimentary response

Sets of small basins intra-calderas and probable relatively immature shallow marine deposits are interpreted as forming part of a tectonically unstable setting of a young extensional environment that characterized the southern Amazonian craton during the Paleoproterozoic. Reworked sediments can accumulate into volcano-tectonic depressions created by the eruption, which often collects an intra-caldera lake (Heiken et al., 2000; Németh et al., 2009; Manville et al., 2009). The sedimentation into intra-volcano shallow-water lacustrine basins would have be facilitated (Fig. 17). The alternation of subaerial to shallow-water sedimentation displayed by the alternation of Lf mS and csG is indicative of this volcano-tectonic depressions, which could be also interpreted as immature marine depressions. Subaerial and subaqueous talus coarse-grained up to finer grained turbidites (dsSt) and suspension deposits formed during quiescent periods into lakes or pounds is also inferred (Bacon et al., 2002). Silica-rich accumulations into shallow water basins (Chipera et al., 2008; Manville et al., 2009) deriving from hydrothermal activity in a dynamic volcanic context is also thought to be responsible for the formation of chert accumulation (Lf bChS). Post caldera uplifting (Fig. 17), resurgence or central volcanism could also contribute to produce new sediments to be reworked and transported. Fluvial erosion and reworking of primary deposits produced wide range of different sediments from localized cross-bedded, well-sorted sand (Lf xsS) and gravel (Lf xsSG) beds to massive clast-supported sand and gravel (Lf csGS, csG) and cobble (Lf csGC) deposits. Fluvial deposits occur throughout all successions, representing periods of stream and river reworking and re-establishment after an eruptive phase (Zernack et al., 2011; Roverato et al., 2017). Debris-flows, hyperconcentrated flows, sheet-floods and active sandy braided river systems existed and the absence of vegetation during the Precambrian (Oberholzer and Eriksson, 2000; Roverato et al., 2017) permitted that copious rainfalls easily reworked the available sediments.

11. Conclusion

This study is the result of the lithofaciological analysis carried out during the 2013, 2014 and 2015 field campaigns in the Amazon Craton in the TMP and SFX regions and the successive geochemical and geochronological analysis of samples collected in the field. This work constitutes a further step ahead toward the comprehension of significance, chronostratigraphic distribution and the dynamic of eruption and emplacement of felsic volcanic products in the region. Our results complete previous studies and confirm that products present in the Amazonia Craton could be related either to caldera-type systems (e.g. Lamarão et al., 2002; Juliani et al., 2005; Lamarão et al., 2005; Pierosan et al., 2011) and to fissure-fed eruptive environment following the model proposed by Aguirre-Diaz and Labarthe-Hernández (2003) for the "Sierra Madre Occidental" formation and by Juliani and Fernandes (2010) for the Xingu region. The two models are in fact very similar only differing for the size of the hypothesized magma chambers and the shape of the fissural vents. The described volcano-sedimentary sequences that were characterized by the emission of large volcanic felsic products were likely formed in a late-/post-orogenic (~2 Ga) to extensional regimes (~1.88 Ga).

Acknowledgments

This work was supported by the project CAPES/CNPq 402564/2012-0 (Programa Ciências sem Fronteiras) to Caetano Juliani and Matteo Roverato. M. Roverato acknowledges the grant of the Brasilian CAPES/CNPq Programa Ciências Sem Fronteiras, Atração de Jovem Talento 402564/2012-0. We acknowledge the CNPq/CT-Mineral (Proc. 550.342/2011-7) and the INCT-Geociam (573733/2008-2) — (CNPq/MCT/FAPESPA/PETROBRAS). Furthermore, the first author would like to thank Jeovaci Jr. Martins da Rocha, Diego Felipe Gomez Gutierrez, Lucas Villela Cassini for the help in the field and Carlos Marcelo Diaz Fernandez for the help and very useful discussions. Dr. Giordano acknowledges the financial support for this research from the CAPES project (proposal 302827) of the Ciências Sem Fronteiras program (Brazil) and the local research funds (2012, 2013, 2014) of the University of Turin (Ex60-2015). We are indebted to Nils Lenhardt and Roberto Dall'Agnol for the dedication in reviewing this manuscript and important comments and reviews, which improved considerably this work.

Appendix A. Supplementary data

Supplementary data to this article can be found online at https://doi.org/10.1016/j.gr.2018.12.005.

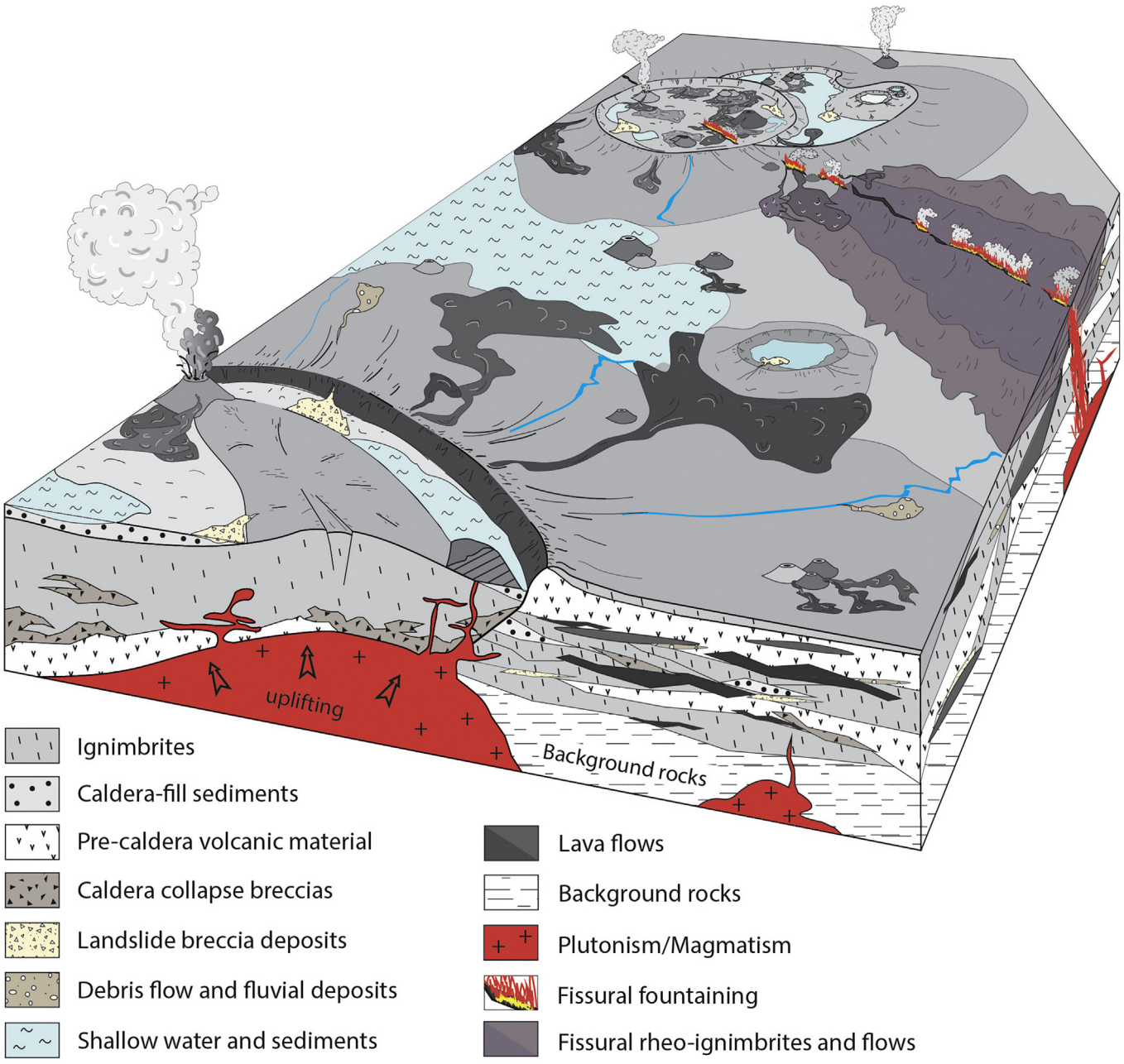

Fig. 17. Peleogeographic reconstruction of the fissural and calderic volcanic activity during the Late-Paleoproterozoic in the southern part of the Amazonian craton. In the foreground is shown a section of a caldera and a post-caldera ignimbrite uplift that could facilitate the production of new sediments to be reworked and transported. The rising magma could form sporadic intra-caldera domes and volcanic centers as also shown in the background calderas. Reworked sediments can accumulate into volcano-tectonic depressions, which often collects intra-caldera lakes. In the background a fissure-fed volcanism is the responsible of the emission of lava flows and/or high-grade to rheomorphic ignimbrites. Fluvial deposits that occur throughout all successions represent periods of stream and river reworking. The area in punctuated by little scoria cones and maars that contribute to the amount of the fragmental products well represented in the study regions.

References

Aguirre-Diaz, G.J., Labarthe-Hernández, G., 2003. Fissure ignimbrites: fissure-source origin for voluminous ignimbrites of the Sierra Madre Occidental and its relationship with Basin and Range faulting. Geology 31, 773–776.

Aguirre-Diaz, G.J., Labarthe-Hernàndez, G., Tristàn-Gonzàlez, M., Nieto-Obregòn, J., Isaac Gutiérrez-Palomares, I., 2008. The ignimbrite flare-up and graben calderas of the Sierra Madre Occidental, Mexico. In: Martí, J., Gottsman, J. (Eds.), Caldera Volcanism: Analysis, Modelling and Response. Developments in Volcanology vol. 10, pp. 143–180.

Almeida, F.F.M., Hasui, Y., Brito Neves, B.B., Fuck, R.A., 1981. Brazilian structural provinces: an introduction. Earth Science Reviews 17, 1–29.

Almeida, M.E., Brito, M.F.L., Ferreira, A.L., Monteiro, M.A.S., 2000. Projeto Especial Província Mineral do Tapajós. Geologia e recursos minerais da Folha Vila Mamãe Anã (SB.21-V-D). Estados do Pará e Amazonas. CPRM, Brasília (CD-ROM).

Amaral, G., 1974. Geologia Pré-Cambriana da Região Amazônica. Tese de Livre Docência, IG/USP (212 pp.).

Anders, E., Ebihara, M., 1982. Solar system aboundances of the elements. Geochimica et Cosmochimica Acta 46, 2363–2380.

Andrews, G.D.M., Branney, M.J., 2011. Emplacement and rheomorphic deformation of a large, lava-like rhyolitic ignimbrite: Grey's Landing, southern Idaho. Geological Society of America Bulletin 123, 725–743.

Antonio, P., D'Agrella-Filho, M.S., Trindade, R.I.F., Nédélec, A., de Oliveira, D.C., da Silva, F.F., Roverato, M., Lana, C., 2017. Turmoil before the boring billion: paleomagnetism of the 1880–1860 Ma Uatumã event in the Amazonian craton. Gondwana Research 49, 106–129.

Bacon, C.R., Gardner, J.V., Mayer, L.A., Buktenica, M.W., Dartnell, P., Ramsey, D.W., Robinson, J.E., 2002. Morphology, volcanism, and mass wasting in Crater Lake, Oregon. Geological Society of America Bulletin 114, 675–692.

Bachmann, O., Dungan, M.A., Lipman, P.W., 2000. Voluminous lava-like precursor to a major ash-flow tuff: low-column pyroclastic eruption of the Pagosa Peak Dacite, San Juan volcanic field, Colorado. J. Volcanol. Geotherm. Res. 98, 153–171.

Bahia, R.B.C., Quadros, M.L.E.S., 2000. Geologia e recursos minerais da Folha Caracol SB.21-X-C. Estados do Pará e Amazonas. Escala 1:250.000. CPRM, Brasília (2000. 1 CD ROM).

Barreto, C.J.S., Lafonb, J.M., da Rosa Costac, L.T., Fernandes-Limad, E., 2014. Palaeoproterozoic (~1.89 Ga) felsic volcanism of the Iricoumé Group, Guyana Shield, South America: geochemical and Sm-Nd isotopic constraints on sources and tectonic environment. International Geology Review https://doi.org/10.1080/00206814.2014.930800.
Best, M.G., Christiansen, E.H., 1997. Origin of broken phenocrysts in ash-flow tuffs. GSA Bulletin 109 (1), 63–73.
Blatt, H., Middleton, G., Murray, R., 1980. Origin of Sedimentary Rocks. Prentice-Hall, Englewood Cliffs, p. 634.
Branney, M.J., Kokelaar, B.P., 1992. A reappraisal of ignimbrite emplacement: progressive aggradation and changes from particulate to non-particulate flow during emplacement of high-grade ignimbrite. Bulletin of Volcanology 54, 504–520.
Branney, M.J., Kokelaar, P., 2002. Pyroclastic density currents and the sedimentation of ignimbrites. Geol. Soc. Lond. Mem. 27, 143.
Breitkreuz, C., 2013. Spherulites and lithophysae—200 years of investigation on high temperature crystallization domains in silica-rich volcanic rocks. Bulletin of Volcanology 75, 705.
Brito-Neves, B.B., 2011. The Paleoproterozoic in the South-American continent: diversity in the geologic time. Journal of South American Earth Sciences 32, 270–286.
Brown, D.J., Bell, B.R., 2013. The emplacement of a large, chemically zoned, rheomorphic, lava-like ignimbrite: the Sgurr of Eigg Pitchstone, NW Scotland. Journal of the Geological Society 170, 753–767.
Brown, G.C., Thorpe, R.S., Webb, P.C., 1984. The geochemical characteristics of granitoids in contrasting arcs and comments on magma sources. Journal of the Geological Society 141, 413–426.
Bursik, M.I., Woods, A.W., 1996. The dynamics and thermodynamics of large ash flows. Bulletin of Volcanology 58, 175–193.
Capuzzo, N., Wetzel, A., 2004. Facies and basin architectural of the Late Carboniferous Salvan-Dorénaz continental basin (Western Alps, Switzerland/France). Sedimentology 51, 675–697.
Cas, R.A.F., Wright, J.V., 1987. Volcanic Successions, Modern and Ancient. Unwin Hyman, Boston, p. 528.
Cas, R.A.F., Wright, H.M.N., Folkes, C.B., Lesti, C., Porreca, M., Giordano, G., Viramonte, J.G., 2011. The flow dynamics of an extremely large volume pyroclastic flow, the 2.08-Ma Cerro Galán Ignimbrite, NW Argentina, and comparison with other flow types. Bulletin of Volcanology 73, 1583–1609.
Chapin, C.E., Lowell, G.R., 1979. Primary and secondary flow structures in ash-flow tuffs of the Gribbles Run paleovalley, central Colorado. Special Paper Geological Society of America 180, 137–154.
Chipera, S.J., Goff, F., Goff, C.J., Fittipaldo, M., 2008. Zeolitization of intracaldera sediments and rhyolitic rocks in the 1.25 Ma lake of Valles caldera, New Mexico, USA. Journal of Volcanology and Geothermal Research 178, 317–330.
Collinson, J.D., 1966. Antidune bedding in the Namurian of Derbyshire, England. Geologie en Mijnbouw. vol. 45, pp. 262–264.
Collinson, J.D., Thompson, D.B., 1982. Sedimentary Structures. Allen and Unwin, London, p. 194.
Condie, K.C., 2000. Episodic continental growth models: after thoughts and extensions. Tectonophysics 322, 153–162.
Condie, K.C., 2002. Continental growth during a 1.9-Ga superplume event. Journal of Geodynamics 34, 249–264.
Costa, J.B.S., Hasui, Y., 1997. Evolução geológica da Amazônia. In: Costa, M.L., Angélica, R.S. (Eds.), Contribuições à geologia da Amazônia, pp. 16–90.
Da Cruz, R.S., Fernandes, C.M.D., Villas, R.N.N., Juliani, C., Monteiro, L.V.S., Almeida, T.I.R., Lagler, B., Carneiro, C.C., Misas, C.M.E., 2015. A study of the hydrothermal alteration in Paleoproterozoic volcanic centers, São Felix do Xingu region, Amazonian Craton, Brazil, using short-wave infrared spectroscopy. Journal of Volcanology and Geothermal Research 304, 324–335.
Dall'Agnol, R., Lafon, J.M., Macambira, M.J.B., 1994. Proterozoic anorogenic magmatism in the Central Amazonian Craton: geochronological and geochemical aspects. Mineralogy and Petrology 50, 113–138.
Dall'Agnol, R., Costi, H.T., Leite, A.A.S., Magalhães, M.S., Teixeira, N.P., 1999. Rapakivi granites from Brazil and adjacent areas. Precambrian Research 95, 9–39.
Dall'Agnol, R., Teixeira, N.P., Rämö, O.T., Moura, C.A.V., Macambira, M.J.B., Oliveira, D.C., 2005. Petrogenesis of the paleproterozoic, rapakivi, A-type granites of the Archean Carajás metallogenic province, Brazil. Lithos 80, 101–129.
Dall'Agnol, R., da Cunha, I.R.V., Guimarães, F.V., de Oliveira, D.C., Teixeira, M.F.B., Feio, G.R.L., Lamarão, C.N., 2017. Mineralogy, geochemistry, and petrology of Neoarchean ferroan to magnesian granites of Carajás province, Amazonian Craton: the origin of hydrated granites associated with charnockites. Lithos 277, 3–32.
Druitt, T.H., Sparks, R.S.J., 1984. On the formation of calderas during ignimbrite eruptions. Nature 310, 679–681.
Echeverri-Misas, C.M., 2010. Geologia e gênese do depósito de Au-(Cu) do Palito, Província Aurífera do Tapajós. Dissertação de Mestrado, IG/USP.
Eriksson, P.G., Engelbrecht, J.P., Res, M., Harmer, R.E., 1994. The Bushy Bend lavas, a new volcanic member of the Pretoria Group, Transvaal Sequence. South African Journal of Geology 97, 1–7.
Ewart, A., 1982. The mineralogy and petrology of Tertiary-Recent orogenic volcanic rocks: with special reference to the andesitic-basaltic compositional range, 25-95 in. In: Thorp, R.S. (Ed.), Andesites: Orogenic Andesites and Related Rocks. John Wiley and Sons, New York, p. 724.
Faraco, M.T.L., Carvalho, J.M.A., Klein, E.L., 1997. Carta metalogenética da Provéncia Auréfera do Tapajós. In: Costa, M.L.C., Ange'lica, R.S. (Eds.), Contribuiço¯es a` Geologia da Amazônia. vol. 1. Sociedade Brasileira de Geologia, Belém, Brazil, pp. 423–437.
Fernandes, C.M.D., Juliani, C., Monteiro, L.V.S., Lagler, B., Misas, C.M.E., 2011. High-K calc-alkaline to A-type fissure-controlled volcano-plutonism of the São Félix do Xingu region, Amazonian craton, Brazil: exclusively crustal sources or only mixed Nd model ages? Journal of South America Earth Sciences 32 (4), 351–368.
Ferrari, L., Orozco-Esquivel, T., Manea, V.C., Manea, M., 2012. The dynamic history of the Trans-Mexican Volcanic Belt and the Mexico subduction zone. Tectonophysics 522–523, 122–149.
Ferreira, A.L., Almeida, M.E., Brito, M.F.L., Monteiro, M.A.S., 2000. Projeto Especial Província Mineral do Tapajós. Geologia e recursos minerais da Folha Jacareacanga (SB.21-Y-B). Estados do Pará e Amazonas. Escala 1:250.000. Nota explicativa e mapas. CPRM, Brasília (CD ROM).
Ferron, J.M.T.M., Bastos-Neto, A.C., Lima, E.F., Nardi, L.V.S., Costi, H.T., Pierosan, R., Prado, M., 2010. Petrology, geochemistry, and geochronology of Paleoproterozoic volcanic and granitic rocks (1.89–1.88 Ga) of the Pitinga Province, Amazonian Craton, Brazil. Journal of South American Earth Sciences 29, 483–497.
Fink, J., 1983. Structure and emplacement of a rhyolitic obsidian flow: little Glass Mountain, Medicine Highland, northern California. GSA Bulletin 94, 362–380.
Fink, J.H., Manley, C.R., 1987. Origin of pumiceous and glassy textures in rhyolite flows and domes. Geological Society of America Special Papers 212, 77–88.
Fisher, R.V., 1961. Proposed classification of volcaniclastic sediments and rocks. Geological Society of America Bulletin 72, 1409–1414.
French, J.E., Heaman, L.M., Chacko, T., Srivastava, R.K., 2008. 1891–1883 Ma Southern Bastar–Cuddapah mafic igneous events, India: a newly recognized large igneous province. Precambrian Research 160, 308–322.
Giordano, D., Nichols, A.R.L., Dingwell, D.B., 2005. Glass transition temperatures of natural hydrous melts: a relationship with shear viscosity and implications for the welding process. Journal of Volcanology and Geothermal Research 142, 105–118.
Giordano, D., La Felice, S., Arzilli, F., De Cristofaro, S.P., Masotta, M., Polo, L., 2017. Il vulcanismo effusivo acido del Monte Amiata: stima delle condizioni pre- e sin-eruttive ed implicazioni vulcanologiche. Effusive Acidic Volcanism of Monte Amiata: Estimates of Pre- and Syn-eruptive Conditions and Volcanological Implications. Monografia Il Vulcano di Monte Amiata. ISBN: 978-88-99742-32-4, pp. 171–193.
Giovanardi, T., Girardi, V.A.V., Correia, C.T., Sinigoi, S., Tassinari, C.C.G., Mazzucchelli, M., 2015. U-Pb zircons SHRIMP data from the Cana Brava Layered Complex: new constraints for the mafic-ultramafic intrusions of Northern Goiás, Brazil. Open Geosciences 7, 197–206.
Goldfarb, R., Groves, D., Gardoll, S., 2001. Rotund versus skinny orogens: well-nourished or malnourished gold? Geology 29, 539–542.
Gutscher, M.A., Maury, R., Eissen, J.P., Bourdon, E., 2000. Can slab melting be caused by flat subduction? Geology 28, 535–538.
Hanson, R.E., Gose, W.A., Crowley, J.L., Ramezani, J., Bowring, S.A., Bullen, D.S., Hall, R.P., Pancake, J.A., Mukwakwami, J., 2004. Paleoproterozoic intraplate magmatism and basin development on the Kaapvaal Craton: age, paleomagnetism and geochemistry of ~1.93 to ~1.87 Ga post-Waterberg dolerites. South African Journal of Geology 107, 233–254.
Hasui, Y., Haraly, N.L.E., Schobbenhaus, C., 1993. Megaestruturação Pré-Cambriana do território brasileiro baseada em dados geofísicos e geológicos. Geociências 12, 7–31.
Heiken, G., Wohletz, K., 1987. Tephra deposits associated with silicic domes and lava flows. GSA Special Paper. vol. 212.
Heiken, G., Krier, D., McCormick, T., Snow, M.G., 2000. Intracaldera volcanism and sedimentation — Creede caldera, Colorado. In: Bethke, P.M., Hay, R.L. (Eds.), Ancient Lake Creede: Its Volcano-tectonic Setting, History of Sedimentation, and Relation to Mineralization in the Creede Mining District. Geological Society of America Special Paper vol. 346, pp. 127–157 (Boulder, Colorado).
Henry, C.D., Wolff, J.A., 1992. Distinguishing strongly rheomorphic tuffs from extensive silicic lavas. Bull. Volcanol. 54, 171–186.
Hofmann, A.W., 1988. Chemical differentiation of the Earth: the relationship between mantle, continental crust and oceanic crust. EPSL 90, 297–314.
Irvine, T.N., Baragar, W.R.A., 1971. A guide to the chemical classification of the common volcanic rocks. Can. J. Earth Sci. 8, 523–548.
Juliani, C., 2002. Alteração hidrotermal e metalogênese em sistemas vulcano-plutônicos paleoproterozóicos na Província Aurífera do Tapaj, Cráton Sul Amazônico, Pará. Tese de Livre-Docência, IG/USP.
Juliani, C., Fernandes, C.M.D., 2010. Well-preserved Late Paleoproterozoic volcanic centers in the São Félix do Xingu region, Amazonian Craton, Brazil. Journal of Volcanology and Geothermal Research 191, 167–179.
Juliani, C., Rye, R.O., Nunes, C.M.D., Snee, L.W., Correa Silva, R.H., Monteiro, L.V.S., Bettencourt, J.S., Neumann, R., Neto, A.A., 2005. Paleoproterozoic high sulphidation mineralization in the Tapajós gold province, Amazonian Craton, Brazil: geology, mineralogy, alunite argon age, and stable-isotope constraints. Chemical Geology 215, 95–125.
Juliani, C., Vasquez, M.L., Klein, E.L., Villas, R.N., Echeverri-Misas, C.M., Santiago, E.S.B., Monteiro, L.V.S., Carneiro, C.C., Fernandes, C.M.D., Usero, G., 2014. Metalogenia da Província Tapajós. In: Silva, M.G., Jost, H., Kuyumajian, R.M. (Eds.), Metalogênese das Províncias Tectônicas Brasileiras, 1 ed. vol. 1. CPRM — Serviço Geológico do Brasil, pp. 51–90.
Kay, S.M., Godoy, E., Kurtz, A., 2005. Episodic arc migration, crustal thickening, subduction erosion, and magmatism in the south_central Andes. Geological Society of America Bulletin 117, 67–88.
Klein, E.L., Santos, R.A., Fuzikawa, K., Angélica, R.S., 2001. Hydrothermal fluid evolution and structural control of the brittle-style Guarim lode-gold mineralisation, Tapajós Province, Amazonian Craton, Brazil. Mineralium Deposita 36, 149–164.
Klein, E.L., Vasquez, M.L., Rosa-Costa, L.T., Carvalho, J.M.A., 2002. Geology of Paleoproterozoic gneiss- and granitoid-hosted gold mineralization in Southern Tapajós Gold Province, Amazonian Craton, Brazil. International Geology Review 44, 544–558.
Klein, E.L., Rosa-Costa, L.T., Carvalho, J.M.A., 2004. Estudo de inclusões fluidas em veio de quartzo aurífero do prospecto Patinhas, Província Aurífera do Tapajós, Cráton Amazônico. RBG. vol. 34 pp. 59–66.

Klein, E.L., Almeida, M.E., Costa, L.T.R., 2012. The 1.89–1.87 Ga Uatumã Silicic Large Igneous Province, northern South America: Large Igneous Provinces Commission. http://www.largeigneousprovinces.org/12nov, Accessed date: 12 January 2012.
Kolzenburg, S., Giordano, D., Thordarson, T., Höskuldsson, A., Dingwell, D.B., 2017. The rheological evolution of the 2014/2015 eruption at Holuhraun, central Iceland. Bull. Volcanol. 79, 45.
Kuno, H., 1968. Origin of andesite and its bearing on the island arc structure. Bull. Volcanol. 32, 141–176.
Lagler, B., Juliani, C., Pessoa, F.F., Fernandes, C.M.D., 2011. Petrografia e geoquímica das sequências vulcânicas Paleoproterozóicas na região de Vila Tancredo, São Félix do Xingu (PA). SBGq, Congr. Bras. Geoquí., 13, e Simp. Países do Mercosul, 3, Gramado, RS. Anais (CD-ROM).
Lamarão, C.N., Dall'Agnol, R., Lafon, J.M., Lima, E.F., 1999. As associações vulcânicas e plutônicas de Vila Riozinho e Morais Almeida, Província Aurífera do Tapajós, SW do estado do Pará. Simpósio sobre Vulcanismo e Ambientes Associados. 1, Gramado*/RS, Boletim de resumos, p. 93 (in Portuguese).
Lamarão, C.N., Dall'agnol, R., Lafon, J.M., Lima, E.F., 2002. Geology, geochemistry, and Pb-Pb zircon geochronology of the Paleoproterozoic magmatism of Vila Riozinho, Tapajós Gold Province, Amazonian craton, Brazil. Precambrian Research 119, 189–223.
Lamarão, C.N., Dall'agnol, R., Pimentel, M.M., 2005. Nd isotopic composition of Paleoproterozoic volcanic rocks of Vila Riozinho: implications for the crustal evolution of the Tapajós gold province, Amazon craton. Journal of South American Earth Sciences 18, 277–292.
Legros, F., Kelfoun, K., 2000. On the ability of pyroclastic flows to scale topographic obstacles. Journal of Volcanology and Geothermal Research 98, 235–241.
Lenhardt, N., Hornung, J., Hinderer, M., Böhnel, H., Torres-Alvarado, I.S., Trauth, N., 2011. Build-up and depositional dynamics of an arc front volcaniclastic complex: the Miocene Tepoztlan Formation (Transmexican Volcanic Belt, Central Mexico). Sedimentology 58, 785–823.
Lenhardt, N., Eriksson, P., Catuneanu, O., Bumby, A.J., 2012. Nature of and controls on volcanism in the ca. 2.32–2.06 Ga Pretoria Group, Transvaal Supergroup, Kaapvaal Craton, South Africa. Precambrian Research 214–215, 106–123.
Lenhardt, N., Masango, S.M., Jolayemi, O.O., Lenhardt, S.Z., Peeters, G.J., Eriksson, P.G., 2017. The Palaeoproterozoic (~2.06 Ga) Rooiberg Group, South Africa: dominated by extremely high-grade lava-like and rheomorphic ignimbrites? New observations and lithofacies analysis. Journal of African Earth Sciences 131, 213–232.
Lesti, C., Porreca, M., Giordano, G., Mattei, M., Cas, R.A.F., Wright, H.M.N., Folkes, C.B., Viramonte, J., 2011. High-temperature emplacement of the Cerro Galán and Toconquis Group ignimbrites (Puna plateau, NW Argentina) determined by TRM analyses. Bulletin of Volcanology 73, 1535–1565.
Lofgren, G., 1971. Spherulite textures in glassy and crystalline rocks. Journal of Geophysical Research 76, 5635–5648.
Ludwig, K.R., 2009. Isoplot 4.1. A geochronological toolkit for Microsoft Excel. Berkeley Geochronology Center Special Publication. vol. 4, p. 76.
Macambira, E.M.B., Vale, A.G., 1997. Programa Levantamentos Geológicos Básicos do Brasil. São Félix do Xingu. Folha SB-22-Y-B. Estado do Pará, CPRM, Brasília (in Portuguese).
Manea, V.C., Pérez-Gussinyé, M., Manea, M., 2012. Chilean flat-slab subduction controlled by overriding plate thickness and trench rollback. Geology 40 (1), 35–38.
Manley, C.R., 1996. Physical volcanology of a voluminous rhyolite lava flow: The Badlands lava, Owyhee Plateau, southwestern Idaho. J. Volcanol. Geotherm. Res. 71, 129–153.
Manville, V., Németh, K., Kano, K., 2009. Source to sink: a review of three decades of progresss in the understanding of volcaniclastic processes, deposits, and hazards. Sedimentary Geology 220, 136–161.
McPhie, J., Doyle, M., Allen, S.R., 1993. Volcanic Textures: A Guide to the Interpretation of Textures in Volcanic Rocks. Centre for Ore Deposit and Exploration Studies. University of Tasmania, p. 198.
Miall, A.D., 1996. The Geology of Fluvial Deposits: Sedimentary Facies, Basin Analysis, and Petroleum Geology. Springer-Verlag, New York, p. 582.
Minifie, M.J., Kerr, A.C., Ernst, R.E., Hastie, A.R., Ciborowski, T.J.R., Desharnais, G., Millar, I.L., 2013. The northern and southern sections of the western ca. 1880 Ma Circum-Superior Large Igneous Province, North America: the Pickle Crow dyke connection? Lithos 174, 217–235.
Monteiro, L.V.S., Xavier, R.P., de Carvalho, E.R., Hitzman, M.W., Johnson, C.A., de Souza Filho, C.R., Torresi, I., 2008. Spatial and temporal zoning of hydrothermal alteration and mineralization in the Sossego iron oxide-copper-gold deposit, Carajás Mineral Province, Brazil: paragenesis and stable isotope constraints. Mineralium Deposita 43, 129–159.
Mori, P.E., Reeves, S., Correia, C.T., Haukka, M., 1999. Development of a fused glass disc XRF facility and comparison with the pressed powder pellet technique at Instituto de Geociências. Revista Brasileira de Geociencias 29, 441–446.
Mori, L., Gómez-Tuena, A., Cai, Y., Goldstein, S., 2007. Effects of prolonged flat subduction on the Miocene magmatic record of the central Trans-Mexican Volcanic Belt. Chemical Geology 244, 452–473.
Mueller, W.U., Concoran, P.L., 1998. Late-orogenic basins in the Archaean Superior Province, Canada: characteristics and inferences. Sedimentary Geology 120, 177–203.
Navarro, M.S., Andrade, S., Ulbrich, H.H.G.J., Gomes, C.B., Girardi, V.A.V., 2008. The analysis of rare earth elements with ICP-MS in basaltic and related rocks: testing the efficiency of sample decomposition procedures. Geostandards and Geoanalytical Research 32 (2), 167–180.
Németh, K., Cronin, S.J., Stewart, R.B., Charley, D., 2009. Intra- and extra-caldera volcaniclastic facies architecture of a frequently active mafic island-arc volcano, Ambryn Island, Vanuatu. Sedimentary Geology 220, 256–270.
Oberholzer, J.D., Eriksson, P.G., 2000. Subaerial volcanism in the Palaeoproterozoic Heekpoort Formation (Transvaal Supergroup), Kaapvaal craton. Precambrian Research 101, 193–210.
Pearce, J.A., 1996. Sources and settings of granitic rocks. Episodes 19 (4), 120–125.
Pearce, J.A., Harris, N.B.W., Tindle, A.G., 1984. Trace element discrimination diagrams for the tectonic interpretation of granitic rocks. Journal of Petrology 25, 956–983.
Pessoa, M.R., Santiago, A.F., Andrade, A.F., Barreto, E.L., Nascimento, J.O., Santos, J.O.S., Oliveira, J.R., Lopes, R.C., Prazeres, W.V., 1977. Projeto Jamanxim. vol. 1–3. CPRM/DNPM, p. 614.
Pierosan, R., Lima, E.F., Nardi, L.V.S., Bastos Neto, A.C., Campos, C.P., Jarvis, K., Ferron, J.M.T.M., Prado, M., 2011. Geochemistry of Palaeoproterozoic volcanic rocks of the Iricoumé Group, Pitinga Mining District, Amazonian craton, Brazil. International Geology Review 53, 946–979.
Pinho, S.C.C., Fernandes, C.M.D., Teixeira, N.P., Paiva Jr., A.L., Cruz, V.L., Lamarão, C.N., Moura, C.A.V., 2006. O magmatismo paleoproterozóico da região de São Félix do Xingu, Província Estanífera do Sul do Pará: Petrografia e geocronologia. Revista Brasileira de Geociencias 36, 793–802.
Pioli, L., Rosi, M., 2005. Rheomorphic structures in a high-grade ignimbrite: the Nuraxi tuff, Sulcis volcanic district (SW Sardinia, Italy). Journal of Volcanology and Geothermal Research 142, 11–28.
Polo, L.A., Giordano, D., Janasi, V., Freitas-Guimaraes, L., 2017a. Effusive silicic volcanism in in the Paraná Magmatic Province, South Brazil: physico-chemical conditions of storage and eruption and considerations on the rheological behaviour during emplacement. Journal of Volcanology and Geothermal Research 355, 115–135.
Polo, L.A., Janasi, V., Giordano, D., Lima, E.F., Cañon-Tapia, E., Roverato, M., 2017b. Effusive silicic volcanism in the Paraná Magmatic Province, South Brazil: evidence for locally-fed lava flows and domes from detailed field work. Journal of Volcanology and Geothermal Research 355, 204–218.
Quane, S.L., Russell, J.K., 2005. Welding: Insights from high-temperature analogue experiments. Journal of Volcanology and Geothermal Research 142 (1–2), 67–87.
Reis, N.R., Almeida, M.E., Ferreira, A.L., Riker, S.R., 2006. Geologia e Recursos Minerais do Estado do Amazonas. Sistema de Informações Geográficas 1:1.000.000. CPRM, Manaus, p. 144.
Rino, S., Tsuyoshi, K., Windley, B.F., Katayama, I., Motoki, A., Hirata, T., 2004. Major episodic increases of continental crustal growth determined from zircon ages of river sands; implications for mantle overturns in the Early Precambrian. Physics of the Earth and Planetary Interiors 146, 369–394.
Roverato, M., 2016. The Montesbelos mass-flow (southern Amazonian craton, Brazil): a Paleoproterozoic volcanic debris avalanche deposit? Bulletin of Volcanology 78, 49.
Roverato, M., Giordano, D., Echeverri-Misas, C.M., Juliani, C., 2016. Paleoproterozoic felsic volcanism of the Tapajós Mineral Province, Southern Amazon Craton, Brazil. Journal of Volcanology and Geothermal Research 310, 98–106.
Roverato, M., Juliani, C., Marcelo Dias-Fernandes, C., Capra, L., 2017. Paleoproterozoic andesitic volcanismin the southern Amazonian craton, the Sobreiro Formation: new insights from lithofacies analysis of the volcaniclastic sequences. Precambrian Research 289, 18–30.
Russell, J.K., Quane, S.L., 2005. Rheology of welding: inversion of field constraints. Journal of Volcanology and Geothermal Research 142 (1–2), 173–191.
Santos, J.O.S., 2003. Geotectônica dos Escudos da Guiana e Brasil Central. In: Bizzi, L.A., Schobbenhaus, C., Vidotti, R.M., Gonçalves, J.H. (Eds.), Geologia, tectônica e recursos minerais do Brasil. Texto, mapas e SIG. CPRM - Serviço Geológico do Brasil, Brasília, pp. 169–226.
Santos, J.O.S., Hartmann, L.A., Gaudette, H.E., Groves, D.I., McNaughton, N.J., Fletcher, I.R., 2000. A new understanding of the provinces of the Amazon craton based on integration of field mapping and U_Pb and Sm_Nd geochronology. Gondwana Research 3, 453–488.
Santos, J.O.S., Groves, D.I., Hartmann, L.A., Moura, M.A., McNaughton, N.J., 2001. Gold deposits of the Tapajós and Alta Floresta Domains, Tapajós-Parima orogenic belt, Amazon Craton, Brazil. Mineralium Deposita 36, 278–299.
Santos, J.O.S., Van Breemen, O.B., Groves, D.I., Hartmann, L.A., Almeida, M.E., McNaughton, N.J., Fletcher, I.R., 2004. Timing and evolution of multiple Paleoproterozoic magmatic arcs in the Tapajós Domain, Amazon Craton: constraints from SHRIMP and TIMS zircon, baddeleyite and titanite U–Pb geochronology. Precambrian Research 13, 73–109.
Schmincke, H.U., Swanson, D.A., 1997. Laminar viscous flowage structures in ash-flow tuffs from Gran Canaria, Canary Islands. J. Geol. 75, 641–664.
Silva, F.S., Oliveira, D.C., Antonio, P.Y., D'Agrella-Filho, M., Lamarão, C.N., 2016. Bimodal magmatism of the Tucuma area, Carajás Province: U-Pb geochronology, classification and processes. Journal of South American Earth Sciences 72, 95–114.
Simões, M.S., Lima, E.F., Sommer, C.A., Rossetti, L.M.M., 2017. Structures and lithofacies of inferred silicic conduits in the Paraná-Etendeka LIP, southernmost Brazil. Journal of Volcanology and Geothermal Research 355, 319–336.
Sulpizio, R., Mele, D., Dellino, P., La Volpe, L., 2007. Deposits and physical properties of pyroclastic density currents during complex Subplinian eruptions: the AD 472 (Pollena) eruption of Somma-Vesuvius, Italy. Sedimentology 54, 607–635.
Sulpizio, R., Dellino, P., Doronzo, D.M., Sarocchi, D., 2014. Pyroclastic density currents: state of the art and perspective. J. Volcanol. Geotherm. Res. 283, 36–65.
Sumner, J.M., Branney, M.J., 2002. The emplacement history of a remarkable heterogeneous, chemically zoned, rheomorphic and locally lava-like ignimbrite: 'TL' on Gran Canaria. Journal of Volcanology and Geothermal Research 115, 109–138.
Tassinari, C.C.G., Macambira, M.J.B., 1999. Geochronological provinces of the Amazonian craton. Episodes 22, 174–182.
Teixeira, W., Tassinari, C.C.G., Cordani, U.G., Kawashita, K., 1989. A review of the geochronology of the Amazonian craton: tectonic implications. Precambrian Research 42, 213–227.
Teixeira, N.P., Bettencourt, J.S., Moura, C.A.V., Dall'Agnol, R., Macambira, E.M.B., 2002. Archean crustal sources for Paleoproterozoic tin-mineralized granites in the Carajas Province, SSE Para, Brazil: Pb_Pb geochronology and Nd isotope geochemistry. Precambrian Research 119, 257–275.

Teixeira, M.F.B., Dall'Agnol, R., Santos, J.O.S., Oliveira, D.C., Lamarão, C.N., McNaughton, N.J., 2018. Crystallization ages of Paleoproterozoic A-type granites of Carajás province, Amazon craton: constraints from U-Pb geochronology of zircon and titanite. Journal of South American Earth Sciences 88, 312–331.

Teixeira, W., Nelson, J.R., Bettencourt, J.S., Klein, E.L., Oliveira, D.C., 2019. Intraplate Proterozoic magmatism in the Amazonian Craton reviewed: geochronology, crustal tectonics and global matches. Dyke Swarms of the World: A Modern Perspective https://doi.org/10.1007/978-981-13-1666-1_4.

Van Kranendonk, M.J., 2006. Volcanic degassing, hydrothermal circulation and the flourishing of early life on Earth: a review of the evidence from c. 3490–3240 Ma rocks of the Pilbara Supergroup, Pilbara Craton, Western Australia. Earth Science Reviews 74, 197–240.

Vasquez, M.L., Dreher, A.M., 2011. Uma avaliação da estratigrafia dos eventos magmáticos de 1900–1860 Ma do Cráton Amazônico. SBG, Simp. Geol. Amaz. 12, Bol. Res (CD ROM).

Vasquez, M.L., Klein, E.L., Macambira, M.J.B., Santos, A., Bahia, R.B.C., Ricci, P., dos, S.F., Quadros, M.L.E.S., 2000. Geochronology of granitoids, mafic intrusions and mineralizations of the Tapajós Gold Province - Amazonian Craton - Brazil. Inter. Geol. Congr. vol. 31 (Abstracts, CD-ROM).

Vasquez, M.L., Sousa, C.S., Carvalho, J.M.A., 2008. Mapa Geológico e de Recursos Minerais do Estado do Pará, escala 1:1.000.000. Programa Geologia do Brasil, Belém, CPRM.

Walker, G.P.L., 1983. Ignimbrite types and ignimbrite problems. Journal of Volcanology and Geothermal Research 17, 65–88.

Went, D.J., 2016. Alluvial fan, braided river and shallow-marine turbidity current deposits in the Port Lazo and Roche Jagu formations, Northern Brittany: relationships to andesite emplacements and implications for age of the Plourivo-Plouézec Group. Geol. Mag. Cambridge University Press, pp. 1–24.

Whalen, J.B., Currie, K.L., Chappell, B.W., 1987. S-type granites: geochemical characteristics, discrimination and petrogenesis. Contrib. Mineral. Petrol. 95, 407–419.

White, J.D.L., Houghton, B.F., 2006. Primary volcaniclastic rocks. Geological Society of America Bulletin 34, 677–680.

Willcock, M.A.W., Cas, R.A.F., Giordano, G., Morelli, C., 2013. The eruption, pyroclastic flow behaviour, and caldera in-filling processes of the extremely large volume (N1290 km^3), intra- to extra-caldera, Permian Ora (Ignimbrite) Formation, Southern Alps, Italy. Journal of Volcanology and Geothermal Research 265, 102–126.

Williams, I.S., 1998. U-Th-Pb geochronology by ion microprobe. In: McKibben, M.A., Shanks, W.C.P., Ridley, W.I. (Eds.), Applications of Microanalytical Techniques to Understanding Mineralizing Processes. Rev Econ Geol vol. 7. Soc. Econ. Geol, Littleton, pp. 1–35.

Wolff, J.A., Wright, J.V., 1981. Rheomorphism of welded tuffs. Journal of Volcanology and Geothermal Research 10, 13–34.

Wood, D.A., 1980. The application of a ThHfTa diagram to problems of tectonomagmatic classification and to establishing the nature of crustal contamination of basaltic lavas of the British Tertiary Volcanic Province. Earth Planet. Sci. Lett. 50, 11–30.

Zanchetta, G., Sulpizio, R., Di Vito, M.A., 2004. The role of volcanic activity and climate in alluvial fan growth at volcanic areas: an example form southern Campania (Italy). Sedimentary Geology 168, 249–280.

Zernack, A.V., Cronin, S.J., Neall, V.E., Procter, J.N., 2011. A medial to distal volcaniclastic record of an andesitic stratovolcano: detailed stratigraphy of the ring-plain succession of south-west Taranaki, New Zealand. International Journal of Earth Sciences 100, 1937–1966.

Zhao, G., Cawood, P.A., Wilde, S.A., Sun, M., 2002. Review of global 2.1–1.8 Ga orogens: implications for a pre-Rodinia supercontinent. Earth-Science Reviews 59, 125–162.

Zhao, G., Sun, M., Wilde, S.A., Li, S., 2004. A Paleo-Mesoproterozoic supercontinent: assembly, growth and breakup. Earth-Science Reviews 67, 91–123.